

Denisovan, modern human and mouse *TNFAIP3* alleles tune A20 phosphorylation and immunity

Nathan W. Zammit^{1,2,24}, Owen M. Siggs^{1,3,24}, Paul E. Gray^{4,5}, Keisuke Horikawa⁶, David B. Langley^{1,2}, Stacey N. Walters^{1,2}, Stephen R. Daley^{6,18}, Claudia Loetsch¹, Joanna Warren^{1,2}, Jin Yan Yap¹, Daniele Cultrone^{1,2}, Amanda Russell¹, Elisabeth K. Malle¹, Jeanette E. Villanueva¹, Mark J. Cowley^{1,2}, Velimir Gayevskiy¹, Marcel E. Dinger^{1,7}, Robert Brink^{1,2}, David Zahra^{1,2}, Geeta Chaudhri^{6,19}, Gunasegaran Karupiah^{6,20}, Belinda Whittle⁶, Carla Roots⁶, Edward Bertram⁶, Michiko Yamada⁶, Yogesh Jeelall⁶, Anselm Enders⁶, Benjamin E. Clifton⁸, Peter D. Mabbitt⁸, Colin J. Jackson⁸, Susan R. Watson^{9,25}, Craig N. Jenne^{9,21}, Lewis L. Lanier⁹, Tim Wiltshire¹⁰, Matthew H. Spitzer^{11,22}, Garry P. Nolan¹¹, Frank Schmitz^{12,23}, Alan Aderem¹², Benjamin T. Porebski¹³, Ashley M. Buckle¹³, Derek W. Abbott¹⁴, John B. Ziegler^{4,5}, Maria E. Craig^{5,15}, Paul Benitez-Aguirre¹⁵, Juliana Teo¹⁵, Stuart G. Tangye^{1,2}, Cecile King^{1,2}, Melanie Wong¹⁵, Murray P. Cox¹⁶, Wilson Phung¹⁷, Jia Tang¹⁷, Wendy Sandoval¹⁷, Ingrid E. Wertz¹⁷, Daniel Christ^{1,2}, Christopher C. Goodnow^{1,2,24*} and Shane T. Grey^{1,2,24*}

Resisting and tolerating microbes are alternative strategies to survive infection, but little is known about the evolutionary mechanisms controlling this balance. Here genomic analyses of anatomically modern humans, extinct Denisovan hominins and mice revealed a *TNFAIP3* allelic series with alterations in the encoded immune response inhibitor A20. Each *TNFAIP3* allele encoded substitutions at non-catalytic residues of the ubiquitin protease OTU domain that diminished I κ B kinase-dependent phosphorylation and activation of A20. Two *TNFAIP3* alleles encoding A20 proteins with partial phosphorylation deficits seemed to be beneficial by increasing immunity without causing spontaneous inflammatory disease: A20 T108A;I207L, originating in Denisovans and introgressed in modern humans throughout Oceania, and A20 I325N, from an *N*-ethyl-*N*-nitrosourea (ENU)-mutagenized mouse strain. By contrast, a rare human *TNFAIP3* allele encoding an A20 protein with 95% loss of phosphorylation, C243Y, caused spontaneous inflammatory disease in humans and mice. Analysis of the partial-phosphorylation A20 I325N allele in mice revealed diminished tolerance of bacterial lipopolysaccharide and poxvirus inoculation as tradeoffs for enhanced immunity.

Microbial resistance involves innate and adaptive immune responses that prevent, diminish or clear infection, often causing collateral damage to host tissues and increased energy demands. Studies in plants¹ and animals^{2,3} have shown that in some circumstances it can be more efficient for a host to tolerate

microbes rather than resist them. Microbial tolerance involves homeostatic mechanisms to raise thresholds for initiating immune responses, to physically separate microbes from host immune receptors and to repair damage caused directly by microbes or by collateral inflammation^{3–6}. The genetic means by which microbial

¹Garvan Institute of Medical Research, Darlinghurst, New South Wales, Australia. ²Faculty of Medicine, University of New South Wales, Sydney, New South Wales, Australia. ³Department of Ophthalmology, Flinders University, Bedford Park, South Australia, Australia. ⁴Department of Immunology and Infectious Diseases, Sydney Children's Hospital, Randwick, New South Wales, Australia. ⁵School of Women's and Children's Health, University of New South Wales, Sydney, New South Wales, Australia. ⁶John Curtin School of Medical Research, The Australian National University, Canberra, Australian Capital Territory, Australia. ⁷School of Biotechnology and Biomolecular Sciences, University of New South Wales, Sydney, New South Wales, Australia. ⁸Research School of Chemistry, The Australian National University, Canberra, Australian Capital Territory, Australia. ⁹Department of Microbiology & Immunology and the Parker Institute for Cancer Immunotherapy, University of California San Francisco, San Francisco, CA, USA. ¹⁰Eshelman School of Pharmacy, University of North Carolina, Chapel Hill, NC, USA. ¹¹Department of Microbiology & Immunology, Stanford University, Stanford, CA, USA. ¹²Seattle Biomedical Research Institute, Seattle, WA, USA. ¹³Department of Biochemistry and Molecular Biology, Monash University, Clayton, Victoria, Australia. ¹⁴Department of Pathology, Case Western Reserve University School of Medicine, Cleveland, OH, USA. ¹⁵Department of Haematology, The Children's Hospital at Westmead, Westmead, New South Wales, Australia. ¹⁶School of Fundamental Sciences, Massey University, Palmerston North, New Zealand. ¹⁷Genentech Inc., South San Francisco, CA, USA. ¹⁸Present address: Department of Biochemistry and Molecular Biology, Monash University, Clayton, Victoria, Australia. ¹⁹Present address: Research School of Population Health, The Australian National University, Canberra, Australian Capital Territory, Australia. ²⁰Present address: School of Medicine, The University of Tasmania, Hobart, Tasmania, Australia. ²¹Present address: Snyder Institute for Chronic Diseases, University of Calgary, Calgary, Alberta, Canada. ²²Present address: Departments of Otolaryngology and Microbiology & Immunology and the Parker Institute for Cancer Immunotherapy, University of California San Francisco, San Francisco, CA, USA. ²³Present address: Celgene, Seattle, WA, USA.

²⁴These authors contributed equally: Nathan W. Zammit, Owen M. Siggs, Christopher C. Goodnow, Shane T. Grey. ²⁵Deceased: Susan R. Watson.

*e-mail: c.goodnow@garvan.org.au; s.grey@garvan.org.au

resistance and tolerance are balanced remains incompletely understood. Population genetic modeling predicts that resistance traits favor host polymorphism and microbial evasion, whereas microbial tolerance traits tend toward fixation in hosts and microbial mutualism⁷. High mortality in indigenous human populations of Oceania and the Americas exposed to smallpox demonstrates how a tolerated pathogen in its adapted host can cause devastating disease when introduced into non-adapted populations^{8,9}. An example in animals can be seen for European rabbits exposed to myxoma poxvirus, previously endemic to South American rabbits⁸. These cases illustrate the importance of fine-tuning microbial immunity and tolerance during coevolution of hosts and microbes, although little is known about the molecular pathways that underpin this.

A binary perspective on the importance of balancing microbial immunity and tolerance comes from Mendelian gene variants in mice and humans that completely inactivate one or both alleles of genes such as *CTLA4*, *IL10*, *FOXP3* and *TNFAIP3* (refs. 10–12). These variants cause severe pediatric autoimmune or inflammatory disease, particularly at mucosal barriers where large microbial populations are normally tolerated, such as the microbial burden that drives inflammatory pathology in mouse *Tnfaip3* deficiency⁶. Genome-wide and candidate association studies in humans have implicated single-nucleotide polymorphisms at or near the *TNFAIP3* locus in susceptibility to autoimmune disease¹³. In contrast to these disease-associated traits, few examples exist of beneficial genetic adjustments that decrease microbial tolerance in favor of heightened immunity.

A20, encoded by the *TNFAIP3* gene, promotes microbial tolerance as a negative regulator of nuclear factor (NF)- κ B signaling; an evolutionarily ancient and central pathway for activating innate and adaptive immune responses¹³. A20 has multiple domains with inhibitory activity against NF- κ B, primarily preventing activation of the central I κ B kinase (IKK) by upstream proteins RIPK1, TRAF6 and NEMO. The A20 ovarian tumor (OTU) domain has deubiquitinating (DUB) protease activity that cleaves activating K63-linked ubiquitin chains from RIPK1, TRAF6 and NEMO^{14–16}. The A20 zinc finger 7 domain (ZnF7) binds linear polyubiquitin to suppress IKK activation, whereas ZnF4 promotes ligation of K48-linked ubiquitin chains to RIPK1, triggering RIPK1 proteolysis^{14,17}. A20 feedback inhibition is induced at two levels: NF- κ B proteins directly induce *TNFAIP3* mRNA, and the inhibitory activities of A20 protein are enhanced by IKK β -mediated serine phosphorylation near the ZnF domains, notably at S381 (refs. 18,19).

The role of the A20 OTU domain nevertheless remains enigmatic. The ZnF domains alone are sufficient for NF- κ B inhibitory function in cell-based studies^{20,21}, and mice homozygous for *Tnfaip3* missense variants creating a catalytically inactive OTU domain have little^{15,18} or no²⁰ evidence of excessive NF- κ B signaling. Here we demonstrate that anatomically modern human, archaic Denisovan and mouse alleles encoding missense variants in the OTU domain modulate A20 phosphorylation by IKK, serving as a genetically tunable element with profound effects on the balance between microbial tolerance and immunity, and provide evidence of introgression to high frequencies during human history.

Results

An A20 OTU domain allele acquired from Denisovans. Three convergent sequencing studies led us to identify a unique functional class of A20 missense alleles affecting the OTU domain, distinct from the ubiquitin protease catalytic site (Fig. 1a,b and Supplementary Fig. 1a). The allele with the most subtle effect, comprising T108A (rs376205580) and I207L (rs141807543) missense substitutions in *cis*, was identified by whole-genome sequencing in 4 of 85 families in Sydney, Australia. The majority of individuals in our cohort carrying the T108A;I207L allele were healthy family members of Māori or Pacific Islander ancestry. This allele was rare in a public variant

collection (gnomAD r2.0.2) but most frequent among individuals with unassigned ancestry (Supplementary Fig. 1b).

We next traced the global distribution of the T108A;I207L allele using the Simons Genome Diversity Project dataset that includes genome sequence data on 300 individuals representing 142 diverse populations²². An analysis of 279 individuals revealed high frequencies of the T108A;I207L allele, ranging from 25–75%, among people of Island Southeast Asia and Oceania, but an absence of the allele elsewhere in the world (Supplementary Fig. 1c and Supplementary Table 1).

Unlike people from Africa or Eurasia, people in Island Southeast Asia and Oceania acquired up to 5% of their genome from Denisovans: archaic hominins who interbred with modern humans ~50,000 years ago, migrating through Asia to settle the continent of Sahul (now Papua New Guinea and Australia)^{23–26}. Analysis of the high-coverage genome of a Denisovan finger phalanx from a cave in the Altai Mountains of Siberia²⁷ revealed homozygosity for the T108A;I207L allele (Fig. 1c). Both variants were absent from the genome of a Neanderthal who had inhabited the same cave²⁸ (Supplementary Table 2), suggesting that T108A and I207L arose after divergence of the Denisovan and Neanderthal lineages 170,000–700,000 years ago²⁷.

Multiple Denisovan-derived genomic regions, including one encompassing *TNFAIP3*, bear strong signatures of introgression in people from Papua^{25,26,29}. To investigate the geographical distribution of the T108A;I207L allele in finer detail, we made use of genome-wide array data on 514 individuals from indigenous populations across Island Southeast Asia and Oceania³⁰. By phasing and imputing haplotypes across the *TNFAIP3* locus using these genotype array data, and validating our imputation in 481 modern and archaic whole genomes (Supplementary Tables 3 and 4), we found evidence that the Denisovan *TNFAIP3* haplotype was present at high frequencies in modern human populations east of the Wallace Line, a 50-million-year-old faunal boundary separating organisms of Asiatic and Australian origin via deep water channels between the two continental shelves (Fig. 1d,e and Supplementary Fig. 2a–d)³¹. The T108A;I207L allele was absent in almost all populations west of the Wallace Line, yet accounted for 31–48% of the *TNFAIP3* alleles in Wallacean people of Sumba, Flores, Lembata, Alor and Timor, 32–100% of alleles in people from Papua and 15–45% of alleles in people from Vanuatu, Tonga and Samoa (Fig. 1d and Supplementary Table 4).

We observed the same T108A;I207L *TNFAIP3* haplotype in 31/144 (22%) exome-sequenced alleles in Martu Indigenous Australians from the Pilbara region of Western Australia³², implying that haplotype enrichment occurred before the isolation of Indigenous Australian and Papuan populations (Fig. 1d). The high frequency in Polynesia indicates that the Denisovan *TNFAIP3* haplotype was retained after admixture with Austronesian farming populations, expanding from mainland Asia starting ~4,000 years ago³³ in eastern Indonesia and ~3,000 years ago in the Southwest Pacific³⁴.

Of the two coding variants, T108A was not predicted *in silico* to alter A20 function (Phred-scaled combined annotation-dependent depletion (CADD) score of 0.002) and was present in other vertebrate reference genomes, including that of mouse. In contrast, I207 was invariant across most jawed vertebrates and the I207L variant was predicted to be the most deleterious substitution across the Denisovan *TNFAIP3* haplotype (Phred-scaled CADD score of 23.2; Supplementary Figs. 1a and 2e). Aside from the two missense variants in the introgressed Denisovan *TNFAIP3* haplotype, other noncoding variants could conceivably modulate transcription. Deep sequencing of cDNA nevertheless revealed equal amounts of *TNFAIP3* mRNA from Denisovan and modern human alleles in leukocytes obtained from heterozygous individuals, with or without tumor necrosis factor (TNF) stimulation (Supplementary Fig. 2f).

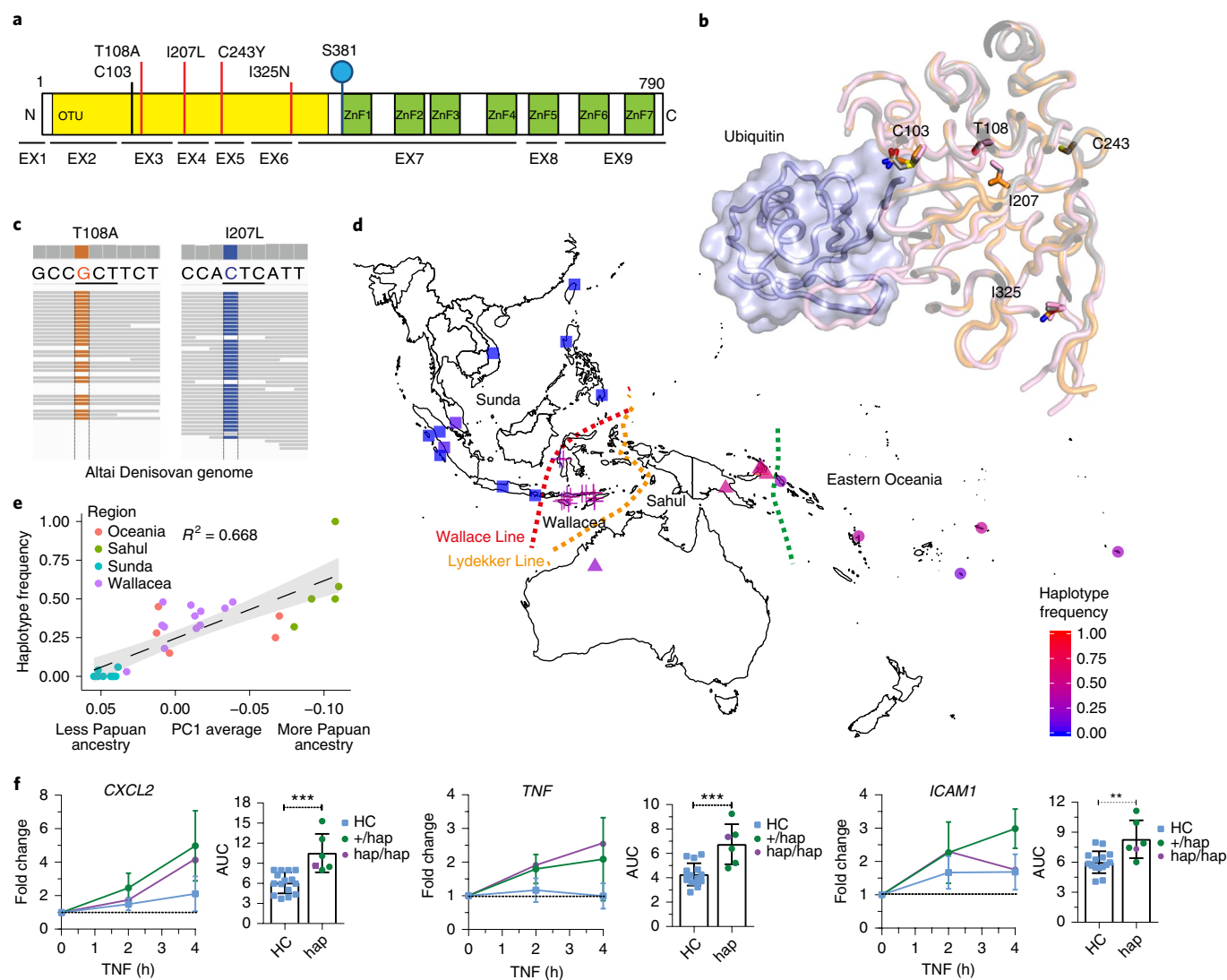


Fig. 1 | Denisoan, modern human and mouse alleles substituting non-catalytic residues of the A20 OTU domain. **a**, Schematic of the A20 protein encoded by the *TNFAIP3* gene (CCDS5187), showing exons (EX1–EX9), OTU, ZnF1–ZnF7, the OTU catalytic residue (C103), the S381 phosphorylation site and the missense substitutions studied here (red lines). **b**, Location of amino acid residues in sliced structure 5LRX⁴¹ of the A20 OTU domain (pink) complexed with ubiquitin (blue). Structures for mouse wild-type 5DQ6 and human I325N OTU 5V3P domains are superposed in gray and orange, respectively. **c**, Read data of a high-coverage Denisoan genome²⁷ across *TNFAIP3* codons 108 and 207. **d**, Imputed frequency of the Denisoan *TNFAIP3* haplotype in genotype array data from 514 individuals from indigenous populations across Island Southeast Asia and Oceania³⁰ and directly observed in exome data from 72 Martu indigenous Australians³². Different symbols group populations from Sunda, Wallacea, Sahul and Eastern Oceania. **e**, Imputed Denisoan *TNFAIP3* haplotype frequency from the populations described in **d** (filled circles) versus a surrogate estimate of Papuan ancestry (principal component 1; Supplementary Fig. 2a,b). Gray shading indicates the 95% confidence interval of a linear regression line. **f**, RT-PCR analysis of *CXCL2*, *TNF* and *ICAM1* expression in PBMCs from individuals heterozygous (green circles) or homozygous (purple circle) for the Denisoan *TNFAIP3* haplotype (hap) and 15 healthy control donors (HCs; blue squares), comparing induction kinetics following stimulation with recombinant human TNF for 0, 2 or 4 h. Fold change was determined by comparing stimulated values against those for nonstimulated PBMC preparations within the same group. Significance between groups was determined by area under the curve (AUC) analysis. Summary data are shown as mean \pm s.d. and *P* values were determined by a two-tailed Student's *t*-test: ***P* < 0.01; ****P* < 0.001.

The Denisoan *TNFAIP3* haplotype was associated with heightened expression of NF- κ B-induced transcripts, including *CXCL2*, *TNF* and *ICAM1*, in TNF-stimulated peripheral blood mononuclear cells (PBMCs) from carriers of the T108A;I207L allele (Fig. 1f, Supplementary Fig. 2g and Supplementary Table 5). The results above identify an ancient pair of substitutions in the A20 OTU domain as apparently beneficial in human history.

A mouse A20 OTU variant confers heightened immunity. Further evidence that A20 OTU domain variants could be beneficial came from another OTU substitution, I325N, identified in a genome-wide

mouse mutagenesis screen in which it segregated with increased frequencies of circulating CD44^{hi} activated/memory T cells and regulatory T cells (Fig. 2a) in otherwise healthy adult mice. Detailed analysis revealed that the I325N allele diminished κ B α levels within most immune cell populations, including T and B cells, natural killer cells, dendritic cells and macrophages (Supplementary Fig. 3a). Macrophages from the bone marrow of mice homozygous for the I325N allele produced more inflammatory cytokines in response to lipopolysaccharide (LPS) than macrophages from wild-type mice (Supplementary Fig. 3b). In isolated thymocytes, presence of the I325N allele increased NF- κ B signaling in ways consistent with

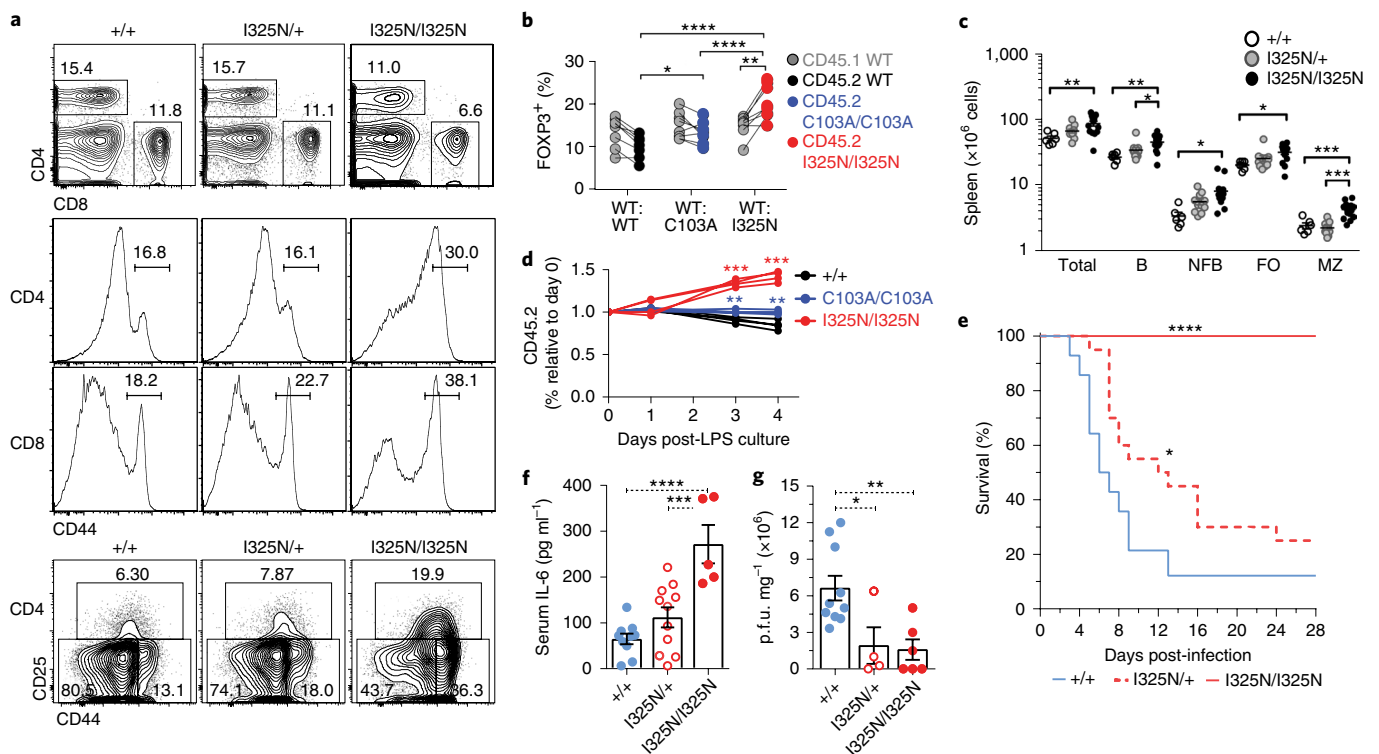


Fig. 2 | The I325N OTU variant confers heightened immunity in mice. **a**, Representative flow cytometry analysis of splenocytes, showing the percentage of CD4⁺ or CD8⁺ T cells and the percentage of CD44^{hi} activated/memory cells within these subsets as well as the percentage of CD25⁺CD44^{int} regulatory T cells and CD25⁺CD44^{int} effector/memory T cells among CD4⁺ cells. **b**, Wild-type (WT) CD45.1⁺ mice were transplanted with mixtures containing equal amounts of congenic bone marrow from CD45.1⁺ donors of *Tnfrap3*^{+/+} genotype and CD45.2⁺ donors of *Tnfrap3*^{I325N/I325N}, *Tnfrap3*^{C103A/C103A} or *Tnfrap3*^{+/+} genotype. A pairwise comparison is shown of the frequency of FOXP3⁺ cells among CD4⁺ splenocytes from the same chimera. **c**, Numbers of the indicated B cells in the spleen of individual mice with the indicated *Tnfrap3* genotype. B, B cells; NFB, newly formed B cells; FO, follicular B cells; MZ, marginal zone B cells. **d**, Splenocytes from the chimeras in **b** were cultured with 0.1 μg ml⁻¹ LPS for 0–4 d, and the frequency of CD45.2⁺ cells of the indicated *Tnfrap3* genotypes was measured among B cells from individual chimeras (lines), expressed relative to the frequency on day 0. **e–g**, Male *Tnfrap3*^{+/+} (*n* = 14), *Tnfrap3*^{I325N/+} (*n* = 20) and *Tnfrap3*^{I325N/I325N} (*n* = 10) C57BL/6 mice were injected with coxsackievirus on day 0. **e**, Kaplan–Meier survival data (two-tailed log-rank test). **f, g**, Plasma IL-6 concentration (**f**) and virus titers (plaque-forming units, p.f.u.) (**g**) per mg of pancreas on day 3. Data are from three independent experiments and are shown as mean ± s.e.m. One-way ANOVA was used for significance analysis unless otherwise stated: **P* < 0.05; ***P* < 0.01; ****P* < 0.001; *****P* < 0.0001.

diminished A20-mediated inhibition (Supplementary Fig. 3c)¹⁸. Furthermore, when wild-type mice were transplanted with mixtures of bone marrow encoding mutant and wild-type A20, the I325N allele acted in a cell-autonomous manner to increase T cell antigen receptor (TCR)- and CD28-dependent formation of FOXP3⁺CD4⁺ regulatory T cells and their Helios⁺FOXP3⁻ precursors within the thymus (Fig. 2b and Supplementary Fig. 3d–f). Mice homozygous for the I325N allele also harbored increased numbers of B cells in the spleen and peritoneal cavity (Fig. 2c and Supplementary Fig. 4a–c). Isolated B cells exhibited increased NF-κB activation in response to both LPS and IgM stimulation (Supplementary Fig. 4d). As for T cells, these responses were found to be cell autonomous, because when wild-type mice were transplanted with mixtures of bone marrow encoding mutant and wild-type A20, only cells harboring the I325N allele exhibited features of increased B cell activation and proliferation by LPS or antigen receptors (Fig. 2d and Supplementary Fig. 4e–g). Surprisingly, I325N had a greater effect than the C103A OTU domain substitution in T cells and B cells analyzed in parallel bone marrow transplant recipients (Fig. 2b,d), despite C103A completely abrogating the polyubiquitin protease activity of A20 (refs. 15,20), indicating that I325N must diminish additional inhibitory mechanisms.

Consistent with heightened levels of cellular markers of immunity, mice with at least one I325N allele of *Tnfrap3* had greater resistance to coxsackievirus B4 strain E2 (hereafter referred to as

coxsackievirus), a virus isolated from a human neonate with a disseminated fatal infection causing extensive pancreatic necrosis^{35,36}. A virus dose that was lethal for 90% of wild-type C57BL/6 mice was not lethal for *Tnfrap3*^{I325N/I325N} littermates, and caused less mortality in *Tnfrap3*^{I325N/+} mice (Fig. 2e and Supplementary Fig. 5a). Mutant mice had less infectious virus and viral RNA in the pancreas, lower levels of mRNA encoding the immune response cytokines interleukin (IL)-1β and interferon-β, less pancreatic necrosis, higher serum IL-6 concentration and preserved body weight and euglycemia (Fig. 2f,g and Supplementary Fig. 5b–g).

The homogeneous genetic background of the *Tnfrap3*-mutant mice allowed testing of whether heightened immunity imposed a subclinical cost or altered the insulin anabolic axis³⁷. *Tnfrap3*^{I325N/+} mice were healthy, of normal weight and fertile, producing homozygous offspring at the expected ratio. Homozygotes also seemed healthy, although their body weights were 5–20% lower than those of their heterozygous and wild-type littermates at 8 and 12 weeks of age (Fig. 3a), with histological analysis revealing low-grade inflammation of the pancreatic islets, colon, kidney and liver (Fig. 3b,c and Supplementary Fig. 6a–i). Pancreatic insulinitis in I325N homozygotes was associated with a 50% reduction in beta cell mass (Fig. 3d), although blood glucose concentrations and glucose tolerance tests were normal (Supplementary Fig. 7a–c). Isolated islets from *Tnfrap3*^{I325N/I325N} mice exhibited normal basal insulin output but

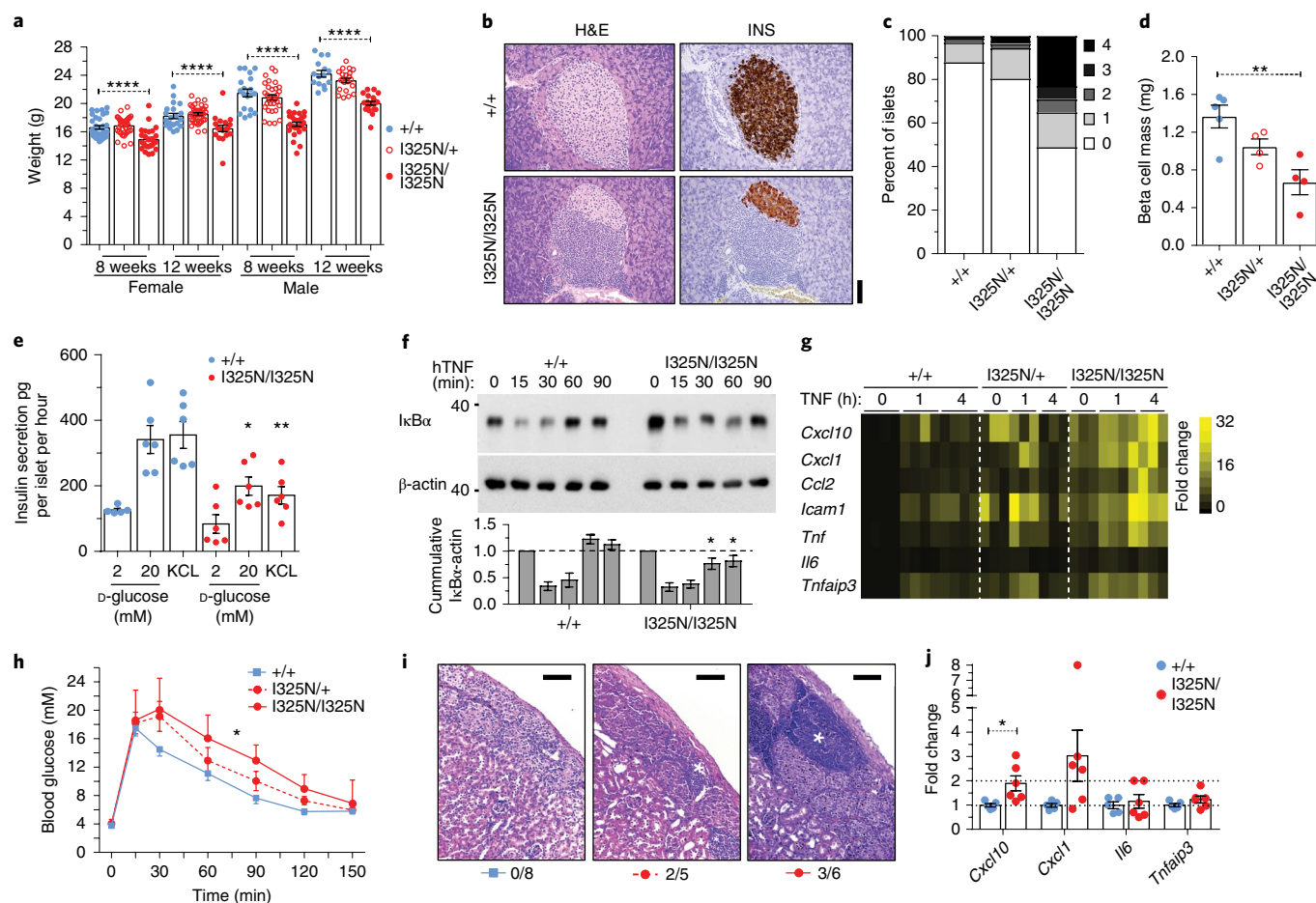


Fig. 3 | Subclinical inflammatory and metabolic consequences of the I325N allele. **a**, Body weights of *Tnfaip3*^{+/+}, *Tnfaip3*^{I325N/+} and *Tnfaip3*^{I325N/I325N} mice of the indicated age and sex. **b**, Hematoxylin and eosin (H&E) and insulin (INS) staining of pancreas sections (scale bar, 100 μ m). **c**, Insulinitis scores (where 4 represents >75% islet mononuclear cell infiltration and 0 represents an absence of infiltrating cells). **d**, Calculated beta cell mass for mice with the *Tnfaip3* I325N allele. Data are representative and cumulative from three independent experiments. **e**, Pancreatic islets were isolated from individual mice of the indicated A20 genotype and incubated overnight. Following incubation, an in vitro glucose-stimulated insulin secretion response assay in 2 mM or 20 mM D-glucose or 25 mM KCl was conducted in separate groups of islets. Cumulative data from three independent experiments are shown. **f, g**, Pancreatic islets were isolated from individual mice of the indicated A20 genotype and treated with 200 U ml⁻¹ TNF for the indicated times. **f**, Representative immunoblot for IkB α and β -actin (loading control). hTNF, recombinant human TNF. **g**, Expression of TNF-induced genes. Data represent three independent islet preparations with four (*Tnfaip3*^{+/+}) and three (*Tnfaip3*^{I325N/I325N}) biological replicates. **h**, Glucose tolerance test in diabetic wild-type mice transplanted with *Tnfaip3*^{+/+} ($n=13$), *Tnfaip3*^{I325N/+} ($n=8$) or *Tnfaip3*^{I325N/I325N} ($n=12$) islets. **i**, Representative H&E sections from three independent experiments of islet grafts at post-operative day 30 (scale bar, 50 μ m), with the fraction of grafts exhibiting immune infiltrate shown below. **j**, Islet grafts isolated on post-operative day 10 were analyzed for the indicated mRNAs by RT-qPCR. Error bars represent mean \pm s.e.m. Statistical analysis was performed by one-way ANOVA (a, d, e, h) or two-tailed Student's *t*-test (j): * $P < 0.05$; ** $P < 0.01$; **** $P < 0.0001$.

reduced insulin secretion when stimulated in vitro (Fig. 3e). Islet transplant and culture experiments showed that the *Tnfaip3* I325N allele acted within islet cells in ways consistent with reduced function, including exaggerating canonical and noncanonical NF- κ B signaling, which lowered insulin secretion and increased inflammatory cytokine gene expression (Fig. 3f–j, Supplementary Figs. 7d,e and 8a–f, and Supplementary Table 6) (ref. 38). Together, these data demonstrate that the A20 I325N allele tunes immunity to provide beneficial protection to coxsackievirus infection at the cost of loss of tissue homeostasis in peripheral tissues, such as the pancreatic islets.

An A20 allelic series shows graded A20 phosphorylation. The apparent beneficial effects of the T108A;I207L and I325N OTU domain alleles detailed above contrasted with the effect of a third OTU domain substitution, A20 C243Y, found as a family-specific allele causing a dominant Mendelian inflammatory disorder resembling Behçet's disease, with childhood onset, oral and genital

ulceration and skin inflammation³⁹. The biochemical basis for the clinically penetrant effects of C243Y was obscure, because other similarly affected cases of A20 haploinsufficiency result from nonsense or frameshift mutations that truncate or eliminate A20 protein¹².

None of the three OTU domain alleles altered the accumulation of A20 protein (Supplementary Fig. 9a), but they nevertheless caused graded reductions in IKK β -mediated phosphorylation of a critical serine residue (S381) that promotes A20 function and NF- κ B inhibition^{18,19} (Fig. 4a–c). The C243Y allele was associated with the most severe loss of IKK β -mediated S381 phosphorylation, diminishing it to 5% of the wild-type level, whereas I325N had an intermediate effect (50% of the wild-type level) and the Denisovan T108A;I207L allele had a mild effect (80% of the wild-type level). Reduced S381 phosphorylation was also observed by mass spectrometry of A20 protein, purified from transfected human cells (Supplementary Fig. 9b). In contrast, the C103A catalytic site substitution did not cause a significant decrease in A20 phosphorylation

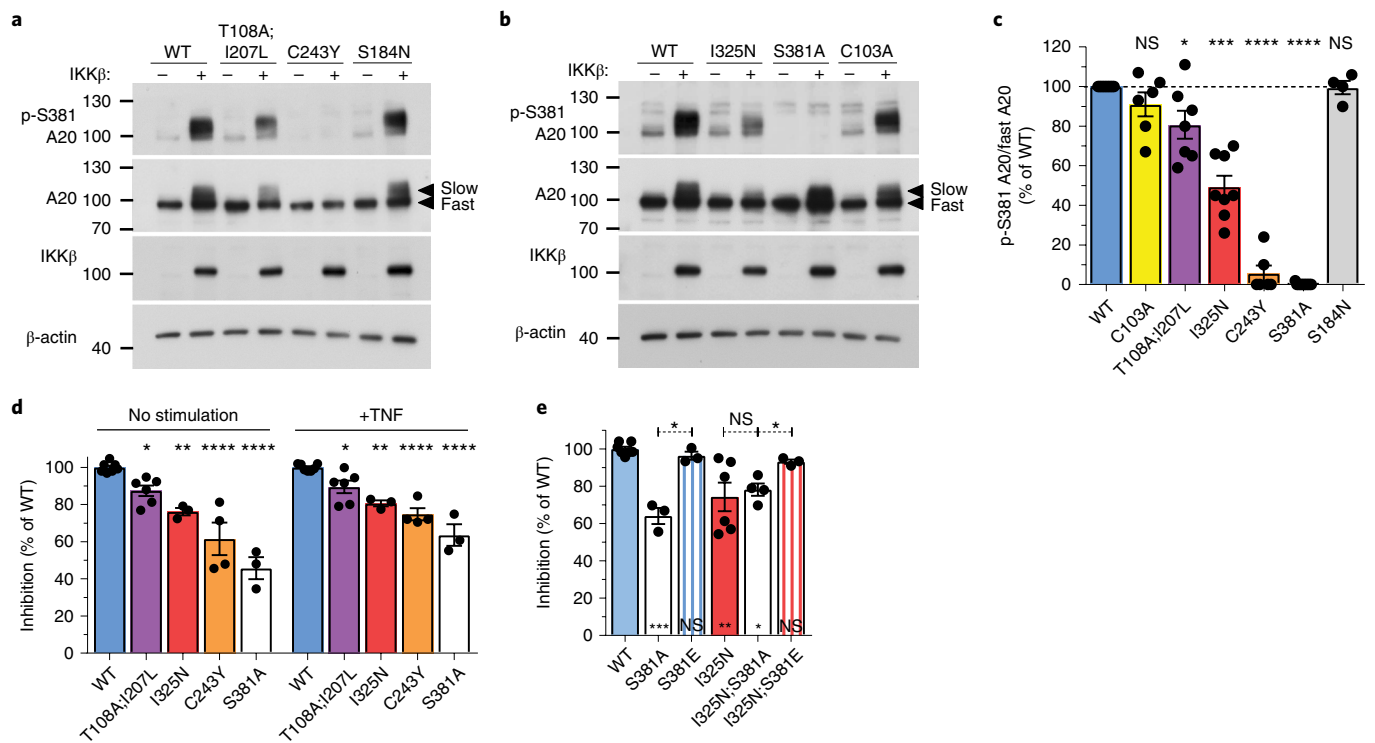


Fig. 4 | Alleles with OTU domain variants decrease A20 phosphorylation and NF- κ B inhibition. **a,b, Representative immunoblots of lysates from β TC3 mouse insulinoma cells transfected with vectors encoding wild-type A20 or A20 with the indicated amino acid substitutions, with or without cotransfected IKK β , and probed with antibodies to p-S381 A20, total A20, IKK β and β -actin. Molecular weight markers (kDa) and slow- or fast-migrating A20 species are indicated. **c**, Densitometric analysis from multiple independent experiments (dots) showing the ratio of p-S381 A20 to total fast-migrating A20 in IKK β -cotransfected cells, expressed relative to the ratio in cells with wild-type A20. NS, not significant. **d,e**, Inhibition of an NF- κ B luciferase reporter in β TC3 cells by cotransfection of wild-type A20 or the indicated A20 mutants, expressed relative to wild-type A20 (Supplementary Fig. 9c,d). Columns are arithmetic means \pm s.e.m. Statistical comparison was performed by one-way ANOVA: * $P < 0.05$; ** $P < 0.01$; *** $P < 0.001$; **** $P < 0.0001$.**

as measured by immunoblotting and mass spectrometry (Fig. 4b,c and Supplementary Fig. 9b).

A20-mediated inhibition of an NF- κ B luciferase reporter was also reduced in a graded fashion by each OTU domain allele in the same order that each diminished S381 phosphorylation (Fig. 4d and Supplementary Fig. 9c). The Denisovan T108A;I207L allele had the smallest effect, whereas the C243Y allele was the poorest NF- κ B inhibitor of the series, with the latter almost as compromised as A20 with S381 substituted to nonphosphorylatable alanine (S381A). Combining the intermediate I325N allele with the S381A mutation in *cis* did not cause a further decrease in A20 activity, consistent with I325N resulting in a primary deficiency in S381 phosphorylation. This conclusion was reinforced by combining I325N in *cis* with a substitution of S381 to the phosphoserine mimetic glutamate (S381E), which rescued the loss of activity caused by I325N (Fig. 4e and Supplementary Fig. 9d).

Phosphorylated A20 (p-S381) predominantly migrated more slowly in SDS-PAGE than unphosphorylated A20, either when tested by cotransfection with IKK β (Fig. 4a,b) or in TNF-stimulated peripheral blood leukocytes with endogenous A20 and IKK β (Fig. 5a). The ratio of this slowly migrating A20 species to the more rapidly migrating form was markedly decreased in blood leukocytes from healthy donors heterozygous for the Denisovan T108A;I207L allele, and further decreased in a healthy donor homozygous for T108A;I207L, as compared to healthy control noncarriers (Fig. 5b). The ratio of p-S381 A20 to fast-migrating A20 was also decreased (Fig. 5c), as was the total level of slow-migrating A20 (Fig. 5d). These biochemical changes had a functional impact, as PBMCs from T108A;I207L carriers showed increased mRNA levels of CXCL2 under unstimulated conditions (Fig. 5e), and a

trend toward increased I κ B α degradation and significantly increased inflammatory gene expression following TNF stimulation (Figs. 1f and 5f).

To explore the structural and biochemical consequences on the posterior surface of the OTU domain, we focused on the intermediate I325N allele. Crystallographic structures of A20 OTU domains with wild-type I325 or mutant N325 revealed no differences in features with known functions, including the catalytic triad and ubiquitin-binding surface (Supplementary Fig. 10a–c and Supplementary Table 7). Subtle shifts in the stem of the β 7– β 8 loop that contains the conserved surface residues T321, T322 and L324 (Supplementary Fig. 10d–f) were detected, but these did not alter the conserved posterior surface of the OTU domain⁴⁰, including the β 3– β 4 loop containing C243 (Supplementary Fig. 10g). The β 7– β 8 loop itself is disordered in all available OTU structures but, like the disordered loops in the unliganded S1 ubiquitin-binding site, it may undergo conformational changes upon binding a cognate partner that are hindered by the I325N substitution⁴¹.

Cycloheximide treatment confirmed no difference in I325N protein stability, and wild-type and I325N OTU domains exhibited similar thermal denaturation profiles (Supplementary Fig. 11a–d). I325N did not decrease the DUB activity of the bacterially expressed OTU domain against K48-linked polyubiquitin in vitro (Supplementary Fig. 11e,f), but did diminish K63-linked polyubiquitin DUB activity and K48-linked ubiquitin ligase activity when full-length A20 was expressed in human cells (Supplementary Fig. 11g,h), consistent with these functions requiring phosphorylation of S381 (refs. 18,19). Together, these data identify a series of A20 OTU domain alleles that cause graded reductions in A20 phosphorylation and A20 control of NF- κ B.

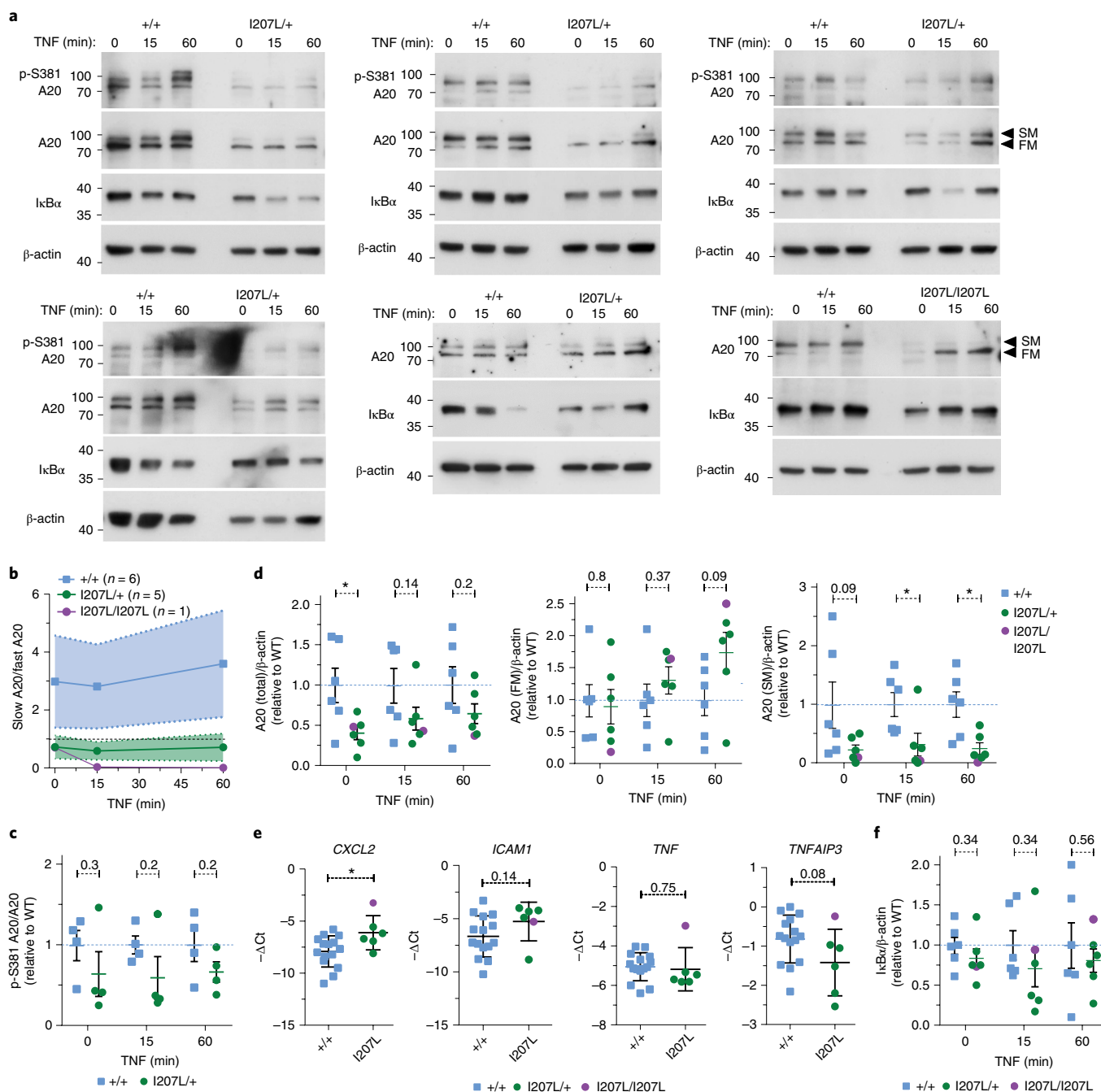


Fig. 5 | Immunoblot and RT-PCR analysis of peripheral blood mononuclear cells from healthy individuals with the Denisovan T108A;I207L TNFAIP3 haplotype. **a**, Immunoblot analysis of PBMCs from individuals with (*TNFAIP3*^{I207L/+}) or without (*TNFAIP3*^{+/+}) the Denisovan *TNFAIP3* haplotype. PBMCs were left untreated or stimulated with hTNF for 15 or 60 min. Proteins assessed included A20, phosphoserine A20 (p-S381 A20), IκBα and β-actin (loading control). **b**, Densitometric ratio of slow- to fast-migrating A20 species, showing the mean and s.d. from six normal donors, five T108A;I207L heterozygotes and one T108A;I207L homozygote. **c**, Densitometry analysis of p-S381 A20 levels in the immunoblots in **a** against the total A20 present. **d**, Densitometry analysis of total A20 levels against β-actin loading control. Data are further divided into fast-migrating (FM) or slow-migrating (SM) A20. **e**, RT-PCR analysis of *CXCL2*, *ICAM1*, *TNF* and *TNFAIP3* gene expression in PBMCs of individuals heterozygous (green circles) or homozygous (purple circle) for the Denisovan *TNFAIP3* haplotype and 15 healthy donors (blue squares), comparing negative ΔCt basal expression levels. **f**, Densitometry analysis of IκBα levels in the immunoblots in **a** corrected for the β-actin loading control. For all densitometry analyses, the average value from samples without the T108A;I207L haplotype was used to compare all samples. Each symbol corresponds to an individual lane in the immunoblot. Error bars represent s.d.; two-tailed Student's *t*-test was used for significance analysis: **P* < 0.05.

Human A20 OTU domain alleles in genome-edited mice. The mouse and human A20 OTU domains show a high degree of secondary and tertiary structural conservation, so to study the physiological effects of human OTU domain alleles in a controlled

genetic and environmental context, human I207L and C243Y alleles were separately introduced into the germline of C57BL/6 mice by CRISPR-Cas9 genome editing. T108A is present in the C57BL/6 mouse and other vertebrate reference genomes, allowing us to

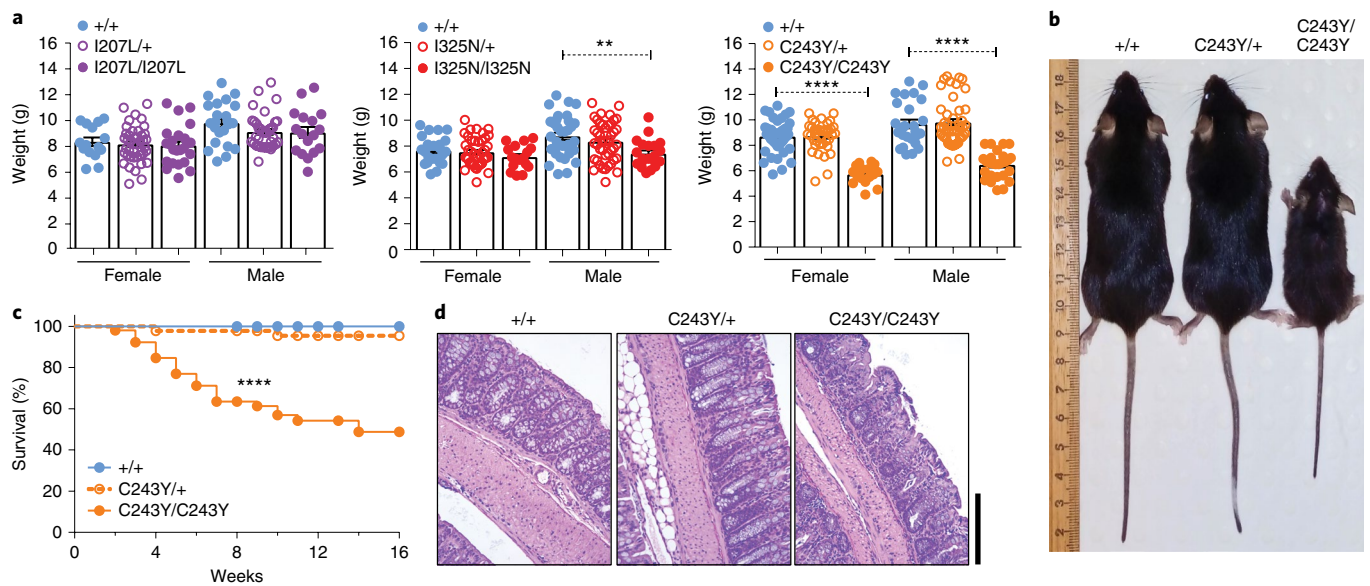


Fig. 6 | C243Y causes spontaneous inflammation and early lethality in homozygous mice. **a**, Weight of 3-week-old *Tnfaip3*^{I207L}, *Tnfaip3*^{I325N} and *Tnfaip3*^{C243Y} mice of the indicated genotype. Bars represent mean \pm s.e.m and one-way ANOVA was conducted to test statistical significance: ***P* < 0.001; *****P* < 0.0001. **b**, Representative photographs of 16-week-old *Tnfaip3*^{C243Y} mice of the indicated genotype. **c**, Survival of mice homozygous for the C243Y allele (*n* = 52) as compared to heterozygous (*n* = 43) and wild-type (*n* = 41) littermates. Significance was determined by two-tailed log-rank test: *****P* < 0.0001. Data are representative sections of three independent experiments, showing H&E-stained colon sections from female mice of the indicated genotype (scale bar, 200 μm).

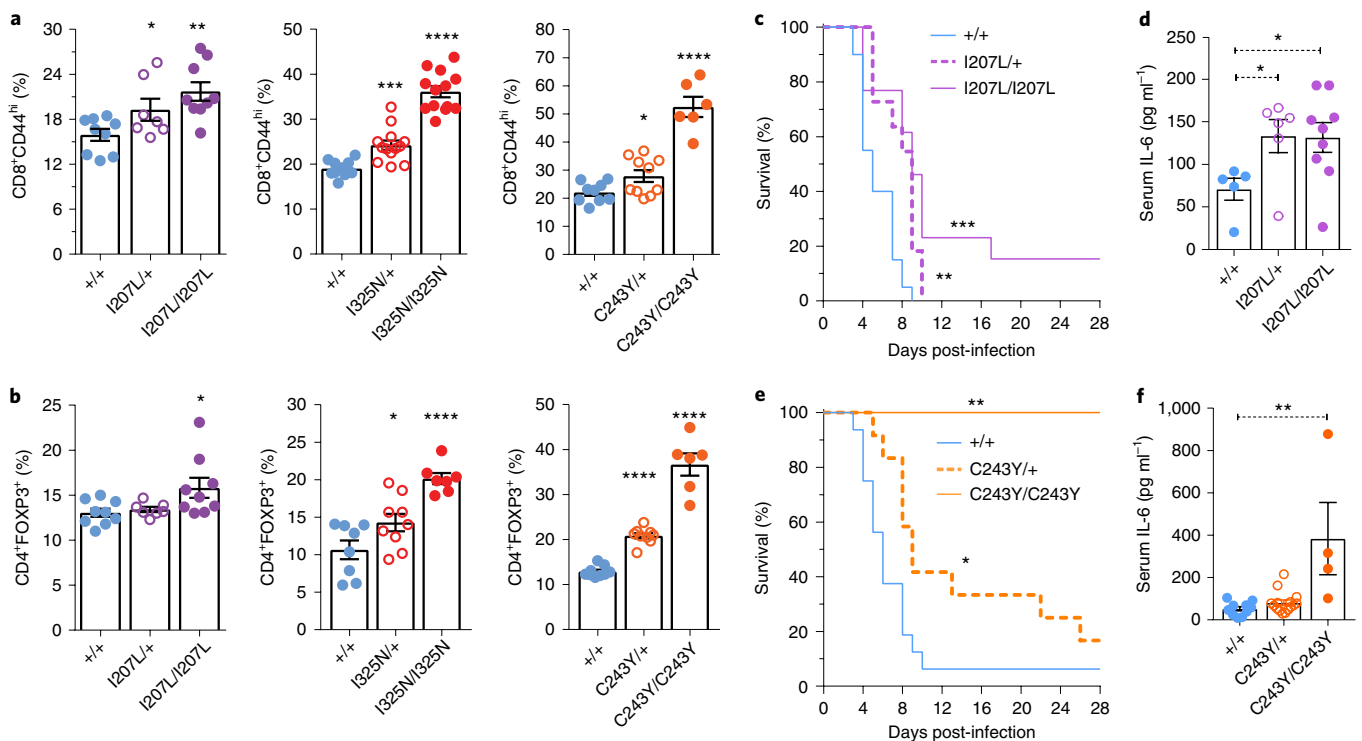


Fig. 7 | Introduction of human T108A;I207L and C243Y alleles in mice tunes immunity. **a**, Percentage of CD44^{hi} activated/memory CD8⁺ T cells. **b**, Percentage of CD4⁺FOXP3⁺ regulatory T cells from the spleens of mice encoding the T108A;I207L (I207L), I325N or C243Y allele. Each point corresponds to an individual mouse collected from more than three independent experiments. Statistical analysis was performed by a two-tailed Student's *t*-test and data are shown as the mean \pm s.e.m: **P* < 0.05; ***P* < 0.01; ****P* < 0.001; *****P* < 0.0001. **c–f**, Male *Tnfaip3*^{+/+} (*n* = 20), *Tnfaip3*^{I207L/+} (*n* = 11), *Tnfaip3*^{I207L/I207L} (*n* = 13) (**c,d**) and *Tnfaip3*^{+/+} (*n* = 16), *Tnfaip3*^{C243Y/+} (*n* = 12) and *Tnfaip3*^{C243Y/C243Y} (*n* = 4) (**e,f**) C57BL/6 mice were injected with coxsackievirus on day 0. **c,e**, Kaplan–Meier survival data (using a two-tailed log-rank test). **d,f**, Plasma IL-6 serum levels on day 3. Data are shown as the mean \pm s.e.m. and one-way ANOVA was used for significance analysis unless otherwise stated: **P* < 0.05.

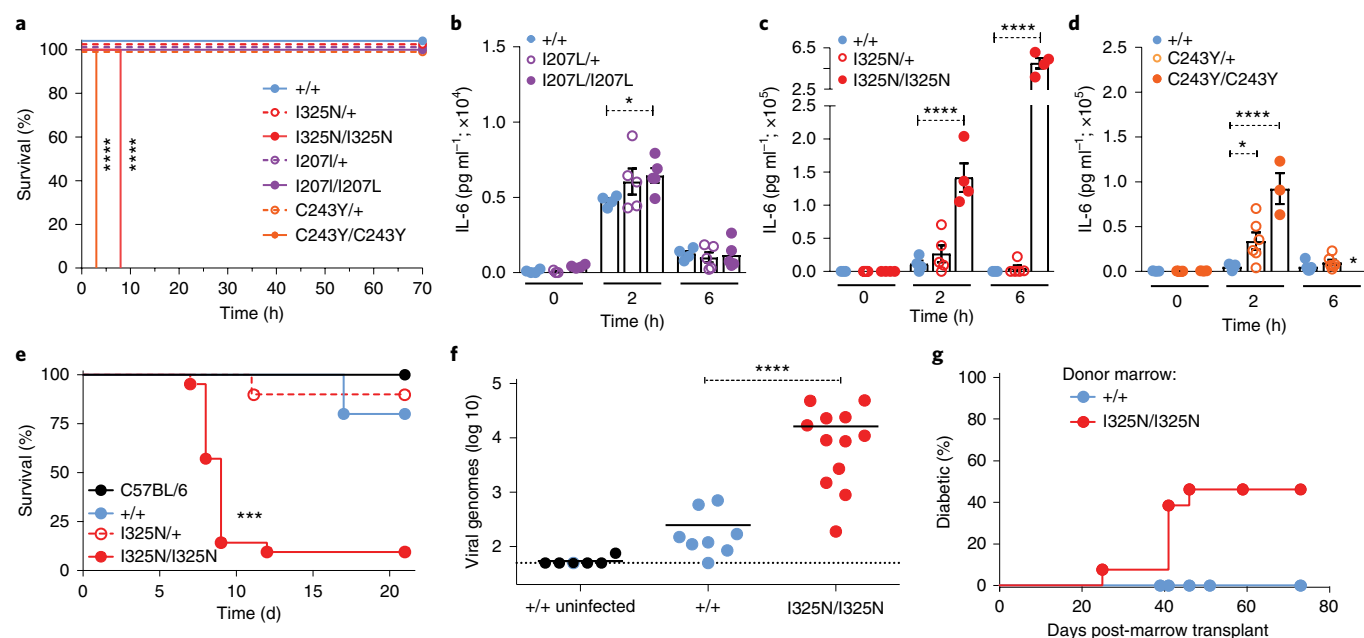


Fig. 8 | Shift to detrimental effects in response to environmental stressors and increased susceptibility to autoimmunity. **a**, Kaplan–Meier survival curves following intraperitoneal injection of 2.5 mg kg⁻¹ LPS in mice harboring the I207L, I325N and C243Y A20 OTU alleles. *Tnfaip3*^{I325N/+} (*n*=16; *Tnfaip3*^{I325N/I325N}, *n*=18; *Tnfaip3*^{I207L/+}, *n*=6 for each genotype; *Tnfaip3*^{C243Y/+}, *n*=5 for each genotype). **b–d**, Serum IL-6 concentration in *Tnfaip3*^{I207L} (**b**), *Tnfaip3*^{I325N} (**c**) and *Tnfaip3*^{C243Y} (**d**) mice of the indicated genotype administered 2.5 mg kg⁻¹ LPS by intraperitoneal injection at time = 0. **e**, Kaplan–Meier survival curves for female littermates of the indicated *Tnfaip3*^{I325N} genotype and wild-type controls (C57BL/6) infected with ectromelia virus. **f**, Day 8 serum viral load assessed from the mice in **e**. **g**, Diminished tolerance to self-antigen caused by I325N A20. The incidence of diabetes is shown in InsHEL transgenic mice with wild-type A20 in pancreatic islets, after transplantation with a congenic bone marrow mixture derived from CD45.1⁺ donors of the *Tnfaip3*^{+/+} genotype transgenic for TCR^{3A9} and CD45.2⁺ donors transgenic for TCR^{3A9} with either the *Tnfaip3*^{I325N/I325N} (red circles) or *Tnfaip3*^{+/+} (blue circles) genotype (*n*=12 chimeras for *Tnfaip3*^{+/+} donors and 14 chimeras for *Tnfaip3*^{I325N/I325N} donors pooled from two separate experiments). Statistical analysis was performed by two-tailed log-rank test (a, e, f) or by one-way ANOVA (b, c, d, f). Bars represent mean ± s.e.m.: **P* < 0.05; ****P* < 0.002; *****P* < 0.0001.

recreate the Denisovan T108A;I207L allele in a single editing step, and also directly test the additive effect of I207L. Mice homozygous for the T108A;I207L allele (*Tnfaip3*^{I207L/I207L}) were born at the expected Mendelian ratio and exhibited no overt signs of illness, weight loss, tissue pathology or early lethality (Fig. 6a and Supplementary Fig. 12a–e). In contrast, mice homozygous for the C243Y allele (*Tnfaip3*^{C243Y/C243Y}) weighed 30–50% less than their wild-type littermates at 3 weeks of age and only ~50% survived to 16 weeks of age (Fig. 6a–c and Supplementary Fig. 12a). Pancreatic and intestinal pathology was also evident in 16-week-old mice homozygous for the C243Y allele, including loss of the goblet cells responsible for maintaining the mucin barrier between the intestinal epithelium and luminal microbes (Fig. 6d and Supplementary Fig. 12c–e).

Comparison of mice with the three different *Tnfaip3* alleles with wild-type littermate controls revealed a graded increase in the frequency of circulating CD44^{hi} activated/memory T cells and FOXP3⁺ regulatory T cells in order of increasing magnitude: I207L heterozygotes < I207L homozygotes = I325N heterozygotes < I325N homozygotes = C243Y heterozygotes < C243Y homozygotes (Fig. 7a,b and Supplementary Fig. 13a–c). Flow cytometry analysis of leukocytes from age-matched and healthy human carriers of the Denisovan T108A;I207L haplotype revealed a subtle increase in CD8⁺ T effector memory cells and T regulatory cells and a significant reduction in the frequency of CD8⁺ effector memory T cells that had re-expressed CD45RA (TEMRA) (Supplementary Fig. 14a–d). CD8⁺ T cells play a key role in viral immunity, and the frequency of CD8⁺ effector memory subsets can reflect the influence of pathogen load and experience^{42,43}. The subtle immune phenotype seen for healthy human carriers was consistent with the graded impact of the T108A;I207L allele on A20 function.

Similarly to *Tnfaip3*^{I325N} mice, *Tnfaip3*^{I207L} and *Tnfaip3*^{C243Y} mice exhibited increased resistance to coxsackievirus (Fig. 7c,e). A virus dose that was lethal for wild-type C57BL/6 mice caused less mortality in *Tnfaip3*^{I207L/I207L} and *Tnfaip3*^{C243Y/+} mice (Fig. 7c,e and Supplementary Information Fig. 1a,b). However, protection was not complete for *Tnfaip3*^{I207L/I207L} mice when compared to *Tnfaip3*^{I325N/I325N} and *Tnfaip3*^{C243Y/C243Y} mice, which showed 100% survival with an otherwise lethal inoculation of coxsackievirus (Figs. 2e and 7c,e). The resistant mice exhibited higher serum IL-6 concentrations, with better preservation of body weight and blood glucose, as compared to wild-type littermates (Fig. 7d,f and Supplementary Information Fig. 1c–f). These data show that the graded reduction in A20 phosphorylation had a physiological impact by beneficially enhancing protective immunity in a correspondingly graded fashion to coxsackievirus.

Shift from beneficial effect to detrimental loss of microbial tolerance. We next explored the possibility that graded loss of A20 phosphorylation and graded loss of microbial tolerance in mice harboring the I325N and C243Y alleles might become detrimental in particular environmental settings. In an experimental model for septic shock, mice homozygous for the I325N and C243Y alleles had higher mortality and greater serum IL-6 concentration following LPS injection as compared to wild-type controls or to T108A;I207L homozygotes (Fig. 8a–d). In the mouse equivalent of smallpox, infection with the orthopoxvirus ectromelia virus was tolerated and controlled by wild-type mice, yet resulted in higher mortality and higher viral titers in I325N homozygotes (Fig. 8e,f and Supplementary Information Fig. 1g,h). Furthermore, in a mouse mixed bone marrow chimera model of autoimmune diabetes,

Table 1 | Comparison of alleles in the A20 OTU allelic series

	Wild type	T108A; I207L	I325N	C243Y
Phred-scaled CADD score (v.1.3)	0	0.002; 23.2	29.2 ^a	25.7
Protein accumulation in transfected cells	1.0	1.0	1.1	1.0
IKK β -driven S381 phosphorylation	100%	81%	49%	6%
Suppression of TNF-stimulated NF- κ B reporter	100%	90%	81%	75%
CD4 ^{hi} CD8 ⁺ T cells	100%	136%	189%	237%
Weight of 8-week-old homozygous mice	Male: 100%; female: 100%	Male: 103%; female: 97%	Male: 79%; female: 90%	Male: 46%; female: 50%
Spontaneous inflammation in homozygous mice	-	-	+	+++
Median survival time after 2.5 mg kg ⁻¹ LPS in homozygous mice	>70 h	>70 h	8 h	3 h
Change in survival time of homozygous mice relative to wild-type littermate controls following coxsackievirus infection	Male: 1; female: 1	Male: 1.8x; female: 1.2x	Male: no deaths; female: no deaths	Male: no deaths; female: no deaths

^aCorresponding human counterpart (6:138198381T>A) to the mouse I325N allele. All values are relative to wild-type controls.

pancreatic islet-reactive CD4⁺ T cells escaped deletion and precipitated diabetes in the presence of cells harboring the I325N allele (Fig. 8g and Supplementary Fig. 15a,b). The rogue islet-reactive T cells were nevertheless derived equally from precursors with wild-type A20 and harboring the I325N allele, whereas I325N acted cell autonomously to increase expression of major histocompatibility complex class II and the T cell co-stimulatory molecule CD86 on B cells and dendritic cells, and to increase the frequencies of germinal center B cells (Supplementary Fig. 15c–e). These data highlight that tuning A20 to increase immunity is balanced by a corresponding cost of increased pathogenicity under different environmental and genetic scenarios, as is most clearly evident with the increasing loss of bacterial tolerance in mice homozygous for I325N and C243Y (summarized in Table 1).

Discussion

Our findings reveal genetic and biochemical mechanisms for adaptively increasing immunity, with tradeoffs against microbial tolerance and anabolic metabolism that either remain clinically silent or become detrimental in specific contexts. Three different alleles altering the N-terminal OTU domain of A20 act, to different degrees, by diminishing A20 phosphorylation, reducing the immune inhibitory activity of A20 *in vitro*, and increasing the frequency of activated T cells and immune responses *in vivo*. A rare human allele, C243Y, almost entirely eliminates A20 phosphorylation and shifts the balance away from microbial tolerance to the extremes of immunity, resulting in severe inflammatory disease in both mice and humans. This outcome is comparable to the phenotypes observed with other rare human alleles that eliminate or truncate the A20 protein expressed from one *TNFAIP3* allele and engineered mouse knockouts that eliminate A20 expression from both alleles^{11,12}. In contrast, the Denisovan T108A;I207L allele, common in people from Oceania, and the chemically induced I325N allele decrease A20 phosphorylation more modestly, without precipitating spontaneous inflammatory disease in the humans or mice who harbor them. Like C243Y, I325N in the mouse confers strong resistance to an otherwise lethal dose of a coxsackievirus, whereas the Denisovan T108A;I207L allele (which has the smallest effect on phosphorylation) confers only partial resistance. Heightened resistance to microbial pathogens may explain the beneficial effect of the Denisovan T108A;I207L *TNFAIP3* haplotype, as evidenced by its high frequency in modern human populations east of the Wallace Line, who likely encountered new pathogens as they moved into environments with unique fauna and flora.

The three *TNFAIP3* alleles analyzed here have much larger effects on immunity in mice than the protease-dead C103A OTU

allele, revealing a previously unanticipated and critical role for the OTU domain in promoting A20 S381 phosphorylation and immune inhibitory activity. Previous studies in mice have conditionally deleted *Tnfaip3* in specific tissues, causing severe inflammatory disease, or directly disabled individual enzymatic functions of A20 in all tissues (for example, via introduction of C103A), resulting in surprisingly little inflammation^{5,6,11,15,18,20}. In contrast, phosphorylation regulates the multiple ubiquitin-editing functions of A20 (refs. ^{18,19}), and as shown here, three OTU domain alleles that diminish phosphorylation have greater effects on immune cells, microbial tolerance and resistance *in vivo* than alleles affecting individual ubiquitin-editing activities. The effects of the three OTU domain alleles on S381 phosphorylation were proportional to their effects on A20 inhibition of NF- κ B signaling and on immunity, and a phosphomimetic substitution (S381E) partially restored the inhibitory function of I325N in an NF- κ B luciferase assay. While these results support the conclusion that the effects are due to the critical role of S381 phosphorylation^{18,19}, they do not exclude the role of other phosphorylation sites or yet-to-be-identified steps activating the inhibitory activities of A20. I207 and T108 are buried deep within the OTU domain, whereas C243 and I325 involve residues within two separate surface loops, β 3– β 4 and β 7– β 8, respectively (Supplementary Fig. 10g), on the highly conserved posterior surface of the OTU domain⁴⁰. Structural studies of full-length A20 protein may illuminate how this surface relates to the C-terminal domain harboring S381. Because the conserved surface bounded by C243 and I325 is large, it potentially offers many opportunities for substitution of buried or surface residues to tune immunity and tolerance.

Our study of the I325N allele with intermediate loss of function provides two examples of genetic tradeoffs. The first involved glucose metabolism, where the I325N allele had the surprising effect within pancreatic islet beta cells of decreasing insulin secretion while increasing inflammation. This is reminiscent of findings in *Drosophila* that insulin production or action decreases during infection, diminishing body glycogen supplies through increased activity of FOXO, a transcriptional inducer of starvation responses³⁷. Resting insulin levels are a good prognostic marker in human sepsis, and exogenous insulin treatment improves outcome⁴⁴. Subtly decreased A20 activity may enhance immune demands for energy and, separately, help meet these energy demands by lowering insulin-induced anabolic growth, contributing to both cachexia associated with chronic infection and inflammation.

The second example of a tradeoff is the experimental demonstration that a beneficial trait in one context can be deleterious in another. The I325N allele conferred increased resistance to

coxsackievirus, an important human enterovirus, but increased mortality to ectromelia virus, a relative of the variola and myxoma viruses. The higher ectromelia virus-related mortality in mice harboring the I325N allele is reminiscent of the high mortality in indigenous populations of the Americas and Oceania exposed to variola virus relative to Europeans⁸. The findings here suggest that the devastation wrought by these and other microbes reflects selection during earlier environmental conditions for lower microbial tolerance and a stronger immune response, with A20 representing one critical determinant of outcome.

Online content

Any methods, additional references, Nature Research reporting summaries, source data, statements of code and data availability and associated accession codes are available at <https://doi.org/10.1038/s41590-019-0492-0>.

Received: 11 September 2018; Accepted: 12 August 2019;

Published online: 18 September 2019

References

- Caldwell, R. M., Schafer, J. F., Compton, L. E. & Patterson, F. L. Tolerance to cereal leaf rusts. *Science* **128**, 714–715 (1958).
- Ayres, J. S. & Schneider, D. S. Tolerance of infections. *Annu. Rev. Immunol.* **30**, 271–294 (2012).
- Soares, M. P., Teixeira, L. & Moita, L. F. Disease tolerance and immunity in host protection against infection. *Nat. Rev. Immunol.* **17**, 83–96 (2017).
- Hooper, L. V., Littman, D. R. & Macpherson, A. J. Interactions between the microbiota and the immune system. *Science* **336**, 1268–1273 (2012).
- Vereecke, L. et al. A20 controls intestinal homeostasis through cell-specific activities. *Nat. Commun.* **5**, 5103 (2014).
- Turer, E. E. et al. Homeostatic MyD88-dependent signals cause lethal inflammation in the absence of A20. *J. Exp. Med.* **205**, 451–464 (2008).
- Roy, B. A. & Kirchner, J. W. Evolutionary dynamics of pathogen resistance and tolerance. *Evolution* **54**, 51–63 (2000).
- Fenner, F. The Florey lecture, 1983. Biological control, as exemplified by smallpox eradication and myxomatosis. *Proc. R. Soc. Lond. B Biol. Sci.* **218**, 259–285 (1983).
- Boughton, C. R. Smallpox and Australia. *Intern. Med. J.* **32**, 59–61 (2002).
- Bousfiha, A. et al. The 2017 IUIS phenotypic classification for primary immunodeficiencies. *J. Clin. Immunol.* **38**, 129–143 (2018).
- Lee, E. G. et al. Failure to regulate TNF-induced NF- κ B and cell death responses in A20-deficient mice. *Science* **289**, 2350–2354 (2000).
- Zhou, Q. et al. Loss-of-function mutations in *TNFAIP3* leading to A20 haploinsufficiency cause an early-onset autoinflammatory disease. *Nat. Genet.* **48**, 67–73 (2016).
- Ma, A. & Malynn, B. A. A20: linking a complex regulator of ubiquitylation to immunity and human disease. *Nat. Rev. Immunol.* **12**, 774–785 (2012).
- Wertz, I. E. et al. De-ubiquitination and ubiquitin ligase domains of A20 downregulate NF- κ B signalling. *Nature* **430**, 694–699 (2004).
- Lu, T. T. et al. Dimerization and ubiquitin mediated recruitment of A20, a complex deubiquitinating enzyme. *Immunity* **38**, 896–905 (2013).
- Evans, P. C. et al. Zinc-finger protein A20, a regulator of inflammation and cell survival, has de-ubiquitinating activity. *Biochem. J.* **378**, 727–734 (2004).
- Bosanac, I. et al. Ubiquitin binding to A20 ZnF4 is required for modulation of NF- κ B signaling. *Mol. Cell* **40**, 548–557 (2010).
- Wertz, I. E. et al. Phosphorylation and linear ubiquitin direct A20 inhibition of inflammation. *Nature* **528**, 370–375 (2015).
- Hutti, J. E. et al. I κ B kinase β phosphorylates the K63 deubiquitinase A20 to cause feedback inhibition of the NF- κ B pathway. *Mol. Cell Biol.* **27**, 7451–7461 (2007).
- De, A., Dainichi, T., Rathinam, C. V. & Ghosh, S. The deubiquitinase activity of A20 is dispensable for NF- κ B signaling. *EMBO Rep.* **15**, 775–783 (2014).
- Verhelst, K. et al. A20 inhibits LUBAC-mediated NF- κ B activation by binding linear polyubiquitin chains via its zinc finger 7. *EMBO J.* **31**, 3845–3855 (2012).
- Mallick, S. et al. The Simons Genome Diversity Project: 300 genomes from 142 diverse populations. *Nature* **538**, 201–206 (2016).
- Reich, D. et al. Genetic history of an archaic hominin group from Denisova Cave in Siberia. *Nature* **468**, 1053–1060 (2010).
- Reich, D. et al. Denisova admixture and the first modern human dispersals into Southeast Asia and Oceania. *Am. J. Hum. Genet.* **89**, 516–528 (2011).
- Sankararaman, S., Mallick, S., Patterson, N. & Reich, D. The combined landscape of Denisovan and Neanderthal ancestry in present-day humans. *Curr. Biol.* **26**, 1241–1247 (2016).
- Vernot, B. et al. Excavating neandertal and denisovan DNA from the genomes of Melanesian individuals. *Science* **352**, 235–239 (2016).
- Meyer, M. et al. A high-coverage genome sequence from an archaic Denisovan individual. *Science* **338**, 222–226 (2012).
- Prüfer, K. et al. The complete genome sequence of a Neanderthal from the Altai Mountains. *Nature* **505**, 43–49 (2014).
- Gittelman, R. M. et al. Archaic hominin admixture facilitated adaptation to out-of-Africa environments. *Curr. Biol.* **26**, 3375–3382 (2016).
- Hudjashov, G. et al. Complex patterns of admixture across the Indonesian archipelago. *Mol. Biol. Evol.* **34**, 2439–2452 (2017).
- Wallace, A. R. On the physical geography of the Malay archipelago. *J. R. Geog. Soc. London* **33**, 217–234 (1863).
- Tang, D. et al. Reference genotype and exome data from an Australian Aboriginal population for health-based research. *Sci. Data* **3**, 160023 (2016).
- Xu, S. et al. Genetic dating indicates that the Asian–Papuan admixture through Eastern Indonesia corresponds to the Austronesian expansion. *Proc. Natl. Acad. Sci. USA* **109**, 4574–4579 (2012).
- Skoglund, P. et al. Genomic insights into the peopling of the Southwest Pacific. *Nature* **538**, 510–513 (2016).
- Kibrick, S. & Benirschke, K. Severe generalized disease (encephalohepatomyocarditis) occurring in the newborn period and due to infection with Coxsackie virus, group B: evidence of intrauterine infection with this agent. *Pediatrics* **22**, 857–875 (1958).
- Hartig, P. C. & Webb, S. R. Heterogeneity of a human isolate of Coxsackie B4: biological differences. *J. Infect.* **6**, 43–48 (1983).
- Dionne, M. S., Pham, L. N., Shirasu-Hiza, M. & Schneider, D. S. Akt and FOXO dysregulation contribute to infection-induced wasting in *Drosophila*. *Curr. Biol.* **16**, 1977–1985 (2006).
- Malle, E. K. et al. Nuclear factor κ B-inducing kinase activation as a mechanism of pancreatic beta cell failure in obesity. *J. Exp. Med.* **212**, 1239–1254 (2015).
- Shigemura, T. et al. Novel heterozygous C243Y A20/*TNFAIP3* gene mutation is responsible for chronic inflammation in autosomal-dominant Behçet's disease. *RMD Open* **2**, e000223 (2016).
- Komander, D. & Barford, D. Structure of the A20 OTU domain and mechanistic insights into deubiquitination. *Biochem. J.* **409**, 77–85 (2008).
- Mevissen, T. E. et al. Molecular basis of Lys11-polyubiquitin specificity in the deubiquitinase Cezanne. *Nature* **538**, 402–405 (2016).
- Appay, V., van Lier, R. A., Sallusto, F. & Roederer, M. Phenotype and function of human T lymphocyte subsets: consensus and issues. *Cytometry A* **73**, 975–983 (2008).
- Appay, V. et al. Memory CD8⁺ T cells vary in differentiation phenotype in different persistent virus infections. *Nat. Med.* **8**, 379–385 (2002).
- van den Berghe, G. et al. Intensive insulin therapy in critically ill patients. *N. Engl. J. Med.* **345**, 1359–1367 (2001).

Acknowledgements

This manuscript is dedicated to the memory of Susan Watson, who led the isolation of the I325N mouse. We thank the National Computational Infrastructure, Xenon systems, Nvidia and the Multi-modal Australian Science Imaging and Visualization Environment (MASSIVE; <http://www.massive.org.au/>) for computing resources. We thank O. Venn, I. Mathieson, B. Llamas, Y. Souilmi, R. Tobler and A. Cooper for stimulating discussions. C.N.J. thanks J. Cyster for mentorship. We thank K. Newton and V. Dixit for reagents (Genentech). We thank M. Flodström-Tullberg (Karolinska Institutet) for kindly providing coxsackievirus B4 strain E2. This study makes use of data generated by the Telethon Kids Institute. A full list of the investigators who contributed to the generation of the data is available from <http://bioinformatics.childhealthresearch.org.au/AGHS>. We thank CIRCA for collecting and coordinating human samples (<http://www.garvan.org.au/research/collaborative-programs/circa/about-circa>). Funding for the project was provided by the National Health and Medical Research Council of Australia (NHMRC) under award 634301. N.W.Z. was supported by an Australian postgraduate award and is supported by the International Pancreas and Islet Transplant Association Derek Gray Scholarship. A.M.B. was an NHMRC Senior Research Fellow (1022688). S.G.T. was a Principal Research Fellow (1042925) of the NHMRC. C.C.G. was supported by the Bill and Patricia Ritchie Chair and by an NHMRC Senior Principal Research Fellowship. S.T.G. was supported by an NHMRC Senior Research Fellowship. The research was supported by grants to C.C.G. from the NIH (AI52127, AI054523, AI100627) and NHMRC (1016953, 585490, 1081858) and to S.T.G. from the NIH (DK076169) and NHMRC (1130222, 1140691). CIRCA was supported by the Jeffrey Modell Foundation, the John Cook Brown Foundation and the Sydney Children's Hospital Network.

Author contributions

Clinical recruitment and genome sequence analyses were conducted by P.G., O.M.S., A.R., J.B.Z., M.E.C., P.B.-A., J.T., M.W., M.J.C., V.G., M.E.D. and C.C.G. Tracing of Denisovan haplotypes in human populations was conducted by O.M.S., P.G., A.R., M.P.C. and C.C.G. Peripheral blood analysis was conducted by N.W.Z., A.R., J.Y.Y., S.G.T., C.C.G. and S.T.G. Identification of I325N mice was conducted by S.R.W., C.N.J., L.L.L., T.W., C.R., B.W. and C.C.G. Immune cell analysis was conducted by N.W.Z., K.H.,

S.R.D., Y.J., M.Y., E.B., A.E., M.H.S., G.P.N., F.S., A.A., I.E.W., S.N.W., S.T.G. and C.C.G. Coxsackievirus studies were carried out by N.W.Z., C.L., J.W., C.K. and S.T.G. Ectromelia studies were conducted by G.C. and G.K. Body weight, islet, LPS and inflammation studies were conducted by N.W.Z., S.N.W., E.K.M., J.E.V. and S.T.G. Protease activity and structural studies were conducted by N.W.Z., D.B.L., K.H., D.C., W.P., I.E.W., B.E.C., P.D.M., C.J.J., B.T.P., A.M.B., S.T.G. and C.C.G. C243Y and I207L mouse strain generation and analysis were conducted by N.W.Z., R.B., D.Z., S.N.W., D.C., J.W., C.C.G. and S.T.G. A20 phosphorylation and NF- κ B luciferase analyses were performed by N.W.Z., D.C., D.W.A., W.P., W.S., J.T., I.E.W., C.C.G. and S.T.G.

Competing interests

W.P., J.T., W.S. and I.E.W. were employees of Genentech. All other authors declare no competing interests.

Additional information

Supplementary information is available for this paper at <https://doi.org/10.1038/s41590-019-0492-0>.

Correspondence and requests for materials should be addressed to C.C.G. or S.T.G.

Peer review information Laurie Dempsey was the primary editor on this article and managed its editorial process and peer review in collaboration with the rest of the editorial team.

Reprints and permissions information is available at www.nature.com/reprints.

Publisher's note Springer Nature remains neutral with regard to jurisdictional claims in published maps and institutional affiliations.

© The Author(s), under exclusive licence to Springer Nature America, Inc. 2019

Methods

Human subjects. Patients and healthy family members were recruited via the Clinical Immunogenomics Research Consortium Australia (CIRCA) and The Children's Hospital at Westmead, providing written informed consent under protocols approved by the Sydney Children's Hospitals Network Human Research Ethics Committee. Blood samples from healthy volunteers were obtained from the Australian Red Cross Blood Service.

Genome sequencing. Parent–proband trio genomes were sequenced on the Illumina HiSeq X platform using DNA isolated from whole blood. Libraries were generated using either Illumina TruSeq PCR-free or TruSeq Nano. Alignment, variant calling and annotation were performed as described previously⁴⁵.

Population genetic analysis. *TNFAIP3* genotypes were extracted from 279 publicly available genomes from Simons Genome Diversity Project samples²⁴ or exome data from 72 Martu Indigenous Australians³². In addition, 514 individuals from across mainland and Island Southeast Asia, Papua New Guinea and Oceania were genotyped at 567,096 variants using the Affymetrix Axiom Genome-Wide Human Array, and the 538,139 autosomal variants with <5% missing data were kept for further analyses³⁰. Weir and Cockerham's estimated F_{ST} values were calculated using VCFtools v.0.1.14, and principal-component analysis was performed using PLINK v.1.9. Genotypes were phased and imputed using the Michigan Imputation Server v.1.0.3 (<http://imputationserver.sph.umich.edu>) and compared to high-coverage Denisovan²⁷ and Altai Neanderthal²⁸ *TNFAIP3* haplotypes. Phred-scaled CADD scores were calculated for all PASS variants across the extended Denisovan haplotype with gnomAD allele frequency <0.01.

To validate the imputation efficiency of the Denisovan T108A and I207L missense variants, we made use of a combined dataset of 481 modern and archaic genomes, including 161 high-coverage genomes from the Indonesian Genome Diversity Project, sampled from 14 islands across Island Southeast Asia⁴⁶. Also included were 292 genomes from the Simons Genome Diversity Project²², 25 additional Papuan genomes⁴⁷, and 2 archaic genomes (Altai Denisovan²⁷ and Neanderthal²⁸). The combined dataset was phased using read-aware phasing with SHAPEIT v.2.r837 (ref. ⁴⁸), using the HapMap phase II b37 recombination map⁴⁹ and the following arguments: --states 400 --window 0.5 --states-random 200. Informative phased genotypes across the interval (chr.6:138160825–138246614) were then segregated into 18 unique haplotypes using Haploview (v.4.2) (ref. ⁵⁰) and used to impute *TNFAIP3* variants in 514 individuals with single-nucleotide polymorphism array data³⁰.

Mice. The *Tnfaip3 lasvegas* strain (*Tnfaip3*^{325SN}) was generated by ENU mutagenesis in C57BL/6 mice, and propagated by backcrossing to C57BL/6 mice. The strain was maintained as heterozygous breeding pairs so that wild-type littermates could be used for controls. To generate *Tnfaip3*^{3243Y} and *Tnfaip3*^{3207L} strains, respective guide RNAs (5'-GGGATATCTGTAACACTCC-3' and 5'-TGACAATGATGGTCTCTGAGG-3') were microinjected into C57BL/6 zygotes in combination with Cas9 mRNA and respective oligonucleotide templates (5'-CACTGTCCTCAGGGTCCACCGGGGTACAAAGTGCTGGCTGCA-TAGCCTAGGACGATGGGATATCTGTAATACCTCTGAGCAGGCCAGT-GAAGAGGCAGATAAATCCACCCACTTTCAAAGGAGCAAAATGGAA CCAGATCCAAAC-3' and 5'-CTCCTCAGAGCTGAAACTCACCCAGGGA-ACCTAGAACTCTCTGAGGCACCTCACCTGAAATGACAATGAGGGG-TCTCTGAGAAATGTTCTGAGGACAAATATGTGGATTCTTCCAGGGA ATTGACTGAAAGTCCACTTCGGGCTGCA-3'). Founder mice carrying the appropriate substitutions were then crossed to C57BL/6 mice, and heterozygous offspring were intercrossed to generate homozygous, heterozygous and wild-type littermates. Mice were housed at the Australian Phenomics Facility (Australian National University) or at the Australian BioResources Centre. *Tnfaip3*^{3203A} (ref. ¹⁸), TCR^{3A9}-transgenic⁵¹ and insHEL transgenic⁵² mice have been described previously. Mice were genotyped for transgenes and A20 by PCR and assessed 7–28 (typically 10–16) weeks after birth. For TCR^{3A9}-transgenic mouse experiments, mice were hemizygous for the 3A9 or insHEL transgene on the B10.BR and B10.BR.SJL-*Ptprc*^u (CD45.1) background, and the *Tnfaip3*^{325SN} mice were backcrossed to B10.BR mice. For bone marrow chimeric mice, congenic C57BL/6.SJL-*Ptprc*^u or B10.BR.SJL-*Ptprc*^u (CD45.1) mice were irradiated with two doses of 4.5 Gy 4 h apart, and injected intravenously with mixtures of 1.8×10^6 bone marrow cells from C57BL/6 or B10.BR.SJL-*Ptprc*^u mice and 1.8×10^6 bone marrow cells from C57BL/6 (CD45.2) mutant or control mice, and analyzed 8–14 weeks later. Animal studies were approved by the Garvan/St Vincent's or the Australian National University Animal Ethics Committees. All procedures performed complied with the Australian Code of Practice for Care and Use of Animals for Scientific Purposes.

Coxsackievirus infection model and virus quantification. Mice were intraperitoneally injected with normal saline (control) or 20 p.f.u. in 200 μ l of saline of the coxsackievirus B4 strain E2 grown in HeLa cells. Mice were monitored daily and euthanized if they displayed gross signs of illness (for example, ruffled coat, hunching). The pancreas was dissected at the indicated times for RT-qPCR, histopathological analysis and viral titer determination. Serum was also collected by terminal cardiac puncture for measurement of IL-6 by ELISA (BD; OptEIA S

et Mouse IL-6), according to the manufacturer's instructions. Plaque assays were performed to determine viral titers within the pancreas following infection. HeLa cells (0.6×10^6 cells per well) were seeded in 2 ml of complete medium (RPMI with 10% FCS, 2 mM L-glutamine, 100 U ml⁻¹ penicillin, 100 μ g ml⁻¹ streptomycin and 100 μ g ml⁻¹ Normocin) in six-well plates and incubated overnight at 37°C. Samples were collected in RPMI, homogenized in a Dounce tissue grinder and passed through a 22- μ m filter, before preparing tenfold serial dilutions. HeLa cells, at 90% confluency, were washed with 1 \times PBS and 400 μ l of infectious homogenate added to each well and incubated for 60 min at 37°C under gentle rocking. Infectious medium was removed and 3 ml of agar mix (2 \times 1.8% agar, 2 \times MEM containing 10% FCS) was added to each well before incubating at 37°C for 3 d. Cells were then fixed with Carnoy's reagent for 60 min and subsequently stained with 0.5% crystal violet for 60 s. Wells were extensively washed with water and plaques were counted.

Ectromelia virus model. Mice were inoculated subcutaneously with 10^3 p.f.u. ectromelia virus (Moscow strain; ATCC no. VR-1374) in the flank of the left hind limb between the regio tarsi and regio pedis under avertin anesthesia. Clinical scores were recorded daily, and animals were weighed on days 0 and 5, and every 2 d thereafter until day 21, and bled on days -1 and 8 to measure viral load. Animals with a significant clinical score or a $\geq 20\%$ decrease in starting weight were euthanized and considered dead the following day. Viral load was measured in the blood by qPCR for *ECTV-Mos-156* viral genomes and in organs by viral plaque assay as the log₁₀ p.f.u. per gram of tissue⁵³.

Macrophage cultures. Bone marrow cells from femurs and tibiae were cultured for 7 d in complete RPMI-1640 medium with 10% FBS, 100 U ml⁻¹ penicillin, 100 μ g ml⁻¹ streptomycin, 2 mM L-glutamine (Life Technologies) and 50 ng ml⁻¹ recombinant human macrophage colony-stimulating factor (PeproTech). Cells were placed into six-well plates for stimulation with 10 ng ml⁻¹ *Salmonella minnesota* R595 (Re) ultra-pure LPS (List Biological) for different periods of time. RNA was extracted by TRIzol (Life Technologies) and reverse transcribed to cDNA with SuperScriptII (Life Technologies), and *Cxcl1* transcript abundance was measured using the TaqMan assay (Applied Biosystems). RNA abundance relative to that of *Efla* was calculated with Δ Ct values. Conditionally *Hoxb8*-immortalized bone marrow progenitor cells were generated as described⁵⁴.

LPS sepsis model. A dose of 2.5 mg kg⁻¹ LPS was administered by intraperitoneal injection. Mice were monitored every 1 h for 10 h and killed if the ethical end point was reached. Monitoring was conducted using body conditioning score and Grimace scale (National Centre for the Replacement, Refinement and Reduction of Animals in Research) approved by the Garvan/St Vincent's Animal Ethics Committee. Monitoring continued twice daily for 7 d in surviving mice, where weights and blood glucose concentrations were also measured. Serum was collected by tail tipping before LPS injection and 2 and 4 h following injection for determination of IL-6 concentration by ELISA (BD, OptEIA Set Mouse IL-6), according to the manufacturer's instructions.

Immunohistochemistry and beta cell area determination. Tissues were fixed in 10% neutral-buffered formalin (Sigma-Aldrich) and embedded in paraffin, and parallel sections (5 μ m) were prepared. Sections were stained with H&E (Sigma-Aldrich) and, for pancreatic tissue, parallel sections were stained for insulin (purified rabbit polyclonal anti-mouse insulin; 4590, Cell Signaling Technology). Visualization of bound anti-insulin was achieved using horseradish peroxidase (HRP)-labeled polymer-conjugated goat anti-rabbit IgG (Dako EnVision+ System), followed by counterstaining with hematoxylin. For pancreatic beta cell mass determination, consecutive pancreatic serial sections at 200- μ m intervals were stained for insulin, and beta cell area was quantified from the total area (taken by insulin-positive cells as compared to nonpositive tissue) (ImageJ, NIH). Beta cell mass (mg) was calculated by multiplying the relative insulin-positive area by the mass of the isolated pancreas before fixation. Images were captured using a Leica DM 4000 or Leica DM 6000 Power Mosaic microscope (Leica Microsystems).

Metabolic studies. Blood glucose concentrations were determined using a FreeStyle Lite glucometer and blood glucose test strips (Abbott Diabetes Care) via tail tipping. Measurements were taken from 8- and 12-week-old male or female non-fasted mice. Glucose tolerance tests and measurements of glucose-stimulated insulin secretion were conducted as previously described⁵⁵.

Islet isolation, transplantation and in vitro studies. Islets were isolated as previously described⁵⁵, and counted for islet transplantation or in vitro experiments using a Leica MZ9.5 stereomicroscope. Islets were transplanted under the kidney capsule of diabetic C57BL/6 littermates as described⁵⁶. For in vitro studies, islets were placed into 12-well non-tissue-culture-treated plates (150–200 islets per well; Fisher Scientific) and were treated with 200 U ml⁻¹ recombinant human TNF (R&D Systems) for 1, 4 or 24 h. Total RNA was extracted using the RNeasy Plus Mini kit (Qiagen) and reverse transcribed using the Quantitect Reverse Transcription kit (Qiagen). Primers were designed using Primer3 (ref. ⁵⁷) with sequences obtained from GenBank and synthesized by Sigma-Aldrich (Supplementary Tables 5 and 6). PCR reactions were performed on the LightCycler480 Real-Time PCR System

(Roche) using FastStart SYBR Green Master Mix (Roche). Cyclophilin (*CPH2*), *RPL13A* and *ACTB* were used as housekeeping genes, and data were analyzed using the $2^{-\Delta\Delta Ct}$ method.

Flow cytometry. Flow cytometry staining was performed as described^{58,59}. Human PBMCs were labeled with the following monoclonal antibodies: anti-CD3 BV421 (UCHT1), anti-CD4 BUV737 (SK3), anti-CD8 BUV379 (RPA-T8) (BD Biosciences); anti-CD127 BV650 (A019D5), anti-CCR7 (CD197) PE-Cy7 (BioLegend); anti-CD25 FITC (2A3) (Becton Dickinson, BD Biosciences) and anti-CD45RA PerCP-Cy5.5 (HI100) (Invitrogen, eBioscience). For mouse lymphocytes, fluorochrome-conjugated antibody clones to the following surface antigens were used: CD4 (RM4-5), CD8 (53-6.7), CD21 (7G6), CD23 (B3B4), CD25 (PC61.5), CD44 (IM7), CD69 (H1.2F3), CD93 (AA4.1), CD45.2 (104), B220 (RA3-6B2), FOXP3 (FJK-165), IgM (II/41), IgD (11-26). B cells were stimulated with: F(ab')₂ goat anti-mouse IgM (10 µg ml⁻¹; Jackson ImmunoResearch Laboratories), LPS from *Escherichia coli* 055:B5 (10, 1.0 or 0.1 µg ml⁻¹; Sigma), anti-CD40 (10 µg ml⁻¹ FGK4.5; BioXCell). TCR^{3A9}-transgenic cells were detected with the 1G12 hybridoma (specific for TCR^{3A9}). Data were acquired with LSRII and FORTRESSA flow cytometers (BD) and analyzed using FlowJo software (Tree Star).

Mass cytometry. Unstimulated spleen cells from four wild-type mice and four mice homozygous for the I325N allele were individually labeled with mass barcodes, mixed, permeabilized and stained with mass-labeled antibodies to a panel of cell-surface markers and intracellular proteins including IκBα, and analyzed by CyTOF⁶⁰. Spanning-tree progression analysis of density-normalized events (SPADE)⁶¹ analysis was used to resolve leukocyte lineages and subsets, and the relative intensity of IκBα in each subset was compared between mutant and wild-type cell counterparts.

Mass spectrometry analysis of A20 phosphorylation at S381. Human and mouse A20 proteins were reduced in sample buffer containing DTT (Sigma) and alkylated in 0.176 M *N*-isopropyliodoacetamide (synthesized in house, mass addition of 99.0684 Da to all cysteine residues). Samples were separated by SDS-PAGE and stained. Bands around 90 kDa in each lane were excised and digested with trypsin as previously described⁶². After overnight digestion, the peptides were extracted from gel slices in acetonitrile and the solution was evaporated to near dryness. Samples were then reconstituted in 10 µl of 0.1% formic acid containing 2% acetonitrile and analyzed by liquid chromatography and tandem mass spectrometry. Reconstituted peptides were injected via an autosampler onto a Dionex UltiMate 3000 RSLCnano Proflow system (Thermo Fisher Scientific) over a gradient of 2% buffer A (98% water and 2% acetonitrile with 0.1% formic acid) to 35% buffer B (98% acetonitrile, 2% water, 0.1% formic acid) and a flow rate of 450 nl min⁻¹. Samples were separated over a 25-cm capillary column (100-µm internal diameter) packed with Waters nanoAcquity M-Class BEH (1.7 µm) material (New Objective). Samples were analyzed online via nanospray ionization into an Orbitrap Fusion Lumos mass spectrometer (Thermo Fisher Scientific). Precursor ion scans were performed in the Orbitrap (resolution of 60,000), and selected peptides were isolated using the quadrupole before fragmentation by high-energy collisional dissociation at a normalized collision energy of 30. The resulting fragment ions were analyzed in the ion trap (resolution of 15,000; AGC target = 2×10^{-4} ; max IT = 11 ms). Tandem mass spectrometry data were searched against candidate sequences using the Byonic and Byologic software packages (Protein Metrics) with variable modifications of oxidation (methionine) and phosphorylation (serine, threonine, tyrosine). AUCs were manually extracted from Xcalibur (Thermo Fisher Scientific).

Immunoblot analysis and immunoprecipitation. Protein concentration was measured using the Bradford assay (Bio-Rad), and total protein (20–25 µg) was resolved on a 7–10% SDS-PAGE gel and then transferred to a nitrocellulose membrane, Immobilon-P (Merck Millipore). Membranes were incubated with anti-IκBα (9242), anti-phospho-IκBα (9256), anti-JNK (9252), anti-phospho-JNK (9255), anti-IKKα (2682), anti-phospho-IKKα/IKKβ (16A6; 2697), anti-NIK (4994), anti-NF-κB2 p100/p52 (4882), anti-RelB (C1E4, 4922, Cell Signaling Technology), anti-β-actin (AC15, Sigma-Aldrich) or anti-S381 A20 (ref. ¹⁹) followed by HRP-labeled secondary goat anti-mouse IgG Fc (Pierce Antibodies) or donkey anti-rabbit IgG (GE Life Sciences). HRP conjugates bound to antigen were detected and visualized by using an ECL detection kit (GE Life Sciences).

For immunoprecipitation anti-TNFR1 (ab7365) or anti-A20 (59A426) antibody (Abcam) were used. Membranes were incubated with anti-A20 (56305/D13H3), anti-IκBα (9242), anti-IKKβ (2684), anti-JNK (9252), anti-TAK1 (52065), anti-phospho-IκBα (9256), anti-phospho-JNK (9255), anti-phospho-TAK1 (4536/90C7), anti-TNFR1 (3736C25C1, Cell Signaling Technology), anti-RIP1 (H-207, Santa Cruz), anti-RIP1 (610458, BD Bioscience), anti-TAK1 (491840, R&D Systems) or anti-β-actin (AC15, Sigma-Aldrich). For B cell stimulation, splenic B cells purified by magnetic-activated cell sorting with CD43 depletion were stimulated with anti-IgM F(ab')₂, or LPS for the indicated times. Cells were lysed with TNE buffer (1% Nonidet P-40, 20 mM Tris-HCl (pH 8.0), 150 mM NaCl, 0.1 mM sodium orthovanadate and complete protease inhibitor; Roche). The following antibodies were used: anti-IκBα (9242), anti-TNFAIP3 (5630/D13H3, C

ell Signaling Technology), anti-A20 (A-12), anti-ubiquitin (P4D1, Santa Cruz Biotechnology) and anti-β-actin (AC15, Sigma-Aldrich).

In vitro reporter transfection studies. Reporter assays were carried out as described previously⁶³. NF-κB activity experiments were conducted using βTC3 cells transfected with 0.3 µg of the NF-κB.Luc reporter (Promega) and 0.2 µg of CMV.β-galactosidase. pcDNA vectors encoding human wild-type or variant A20 constructs or the empty pcDNA3.1 reporter was then added (0.5 µg) to make 1 µg total DNA. Transfection was conducted using Lipofectamine 2000 (Invitrogen). Following transfection, cells were stimulated with 200 U ml⁻¹ of hTNF (R&D Systems). Luciferase activity was assayed in cell lysates collected 8 h after stimulation, using a luciferase assay kit (Promega). Results were normalized to β-galactosidase activity (Galactostar) to give relative luciferase activity. Expression plasmids and reporters were obtained and maintained as described previously⁶³.

Ubiquitination assays. Wild-type A20, A20 I325N or A20 C103A OTU domain protein (1 µg) purified from *E. coli* was added to 2 µg of K48-linked ubiquitin chains of mixed chain length (Ub_n-Ub_n) or to purified tetra-ubiquitin (Ub₄) (UC-230, UC-210, Boston Biochem). Recombinant FLAG-tagged full-length wild-type A20 or A20 I325N was expressed in HEK-293T cells and purified as described previously^{14,17}. Full-length A20 deubiquitination reactions were performed using 100 ng of recombinant A20, 500 ng of the indicated ubiquitin chain and DUB reaction buffer with or without phosphatase inhibitor cocktail and were incubated for the indicated times at 37 °C with agitation at 1,000 r.p.m. Following incubation, samples were placed on ice and 20 µl was collected and added to SDS sample buffer to stop the reaction. A full-length ubiquitin ligase assay was performed as previously described¹⁴. Samples were subjected to one-dimensional SDS-PAGE and immunoblotted for ubiquitin (clone P4D1, Santa Cruz Biotechnology or Cell Signaling Technology) or A20 (clone 59A426, Abcam or A-12, Santa Cruz Biotechnology), as described above.

OTU protein preparation and crystallization. The N-terminal OTU domains of human and mouse A20 (human wild-type and I325N A20, residues 1–366; mouse wild-type and C103A A20, residues 1–360) were cloned into vector pGEX-6P-1 (GE Healthcare), facilitating bacterial expression as a glutathione *S*-transferase (GST) fusion. Expression was performed in *E. coli* strain BL21 (DE3) Gold, where cells were induced at an OD₆₀₀ of 0.5 with 0.2 mM IPTG, followed by incubation at 20 °C overnight in LB medium. Eluted A20 was stabilized with iodoacetamide (Sigma; 30 mM, 30 min at 20 °C, terminated by addition of an equivalent amount of β-mercaptoethanol). For purification of mouse wild-type and C103A proteins, GST-I fusion protein was first eluted (50 mM Tris-HCl (pH 8.0), 200 mM NaCl, 5 mM DTT, 10 mM glutathione) and then the A20 OTU component was released by overnight incubation (4 °C) with PreScission protease. Cleavage products were subjected to anion-exchange chromatography (HiTrap Q FF, GE) where the OTU domain eluted as a single peak between 5 and 500 mM NaCl, 25 mM Tris-HCl (pH 7.5). All proteins were further purified by gel filtration chromatography (AKTA, S200 26/60, buffers as above).

Crystals of both the A20 I325N variant (long triangular rods) and wild-type A20 (long rods) OTU domains grew under the same conditions; equal volumes of protein (2.7 mg ml⁻¹) and well solution (50 mM CaCl₂, 100 mM MES (pH 6.0), 5% PEG1500) were combined in a hanging-drop setup. Crystals grew over several weeks at 20 °C. Cryoprotection was achieved by briefly (for 1–5 s) swimming crystals in mother liquor and doping with glycerol (25% (vol/vol) final) before being plunge vitrified in liquid nitrogen. For mouse wild-type A20, crystallization was achieved by hanging-drop vapor diffusion at a concentration of 8 mg ml⁻¹ in 1.8–2.4 M NaCl, 0.1 M MES (pH 6–6.7). Crystals were soaked in mother liquor containing 30% ethylene glycol for 1 min and immediately vitrified in a nitrogen cryostream.

Crystallographic data reduction and model refinement. Diffraction data were collected at 100 K at beamline MX2 at the Australian Synchrotron and then processed using software as described⁶⁴. Although grown under the same conditions, the crystals for the human wild-type and I325N A20 proteins were in different space groups. The data were highly anisotropic, resulting in poor completeness, low multiplicity and noisy electron density maps. In the case of the mouse OTU crystal, there was marked thermal diffuse scattering. See Supplementary Table 7 for data reduction and refinement statistics.

Structures were solved by molecular replacement using PHASER⁶⁵. The search model was the A-chain of PDB entry 3DKB stripped of surface loops that displayed conformational variability in other PDB entries (2VFJ and 3ZJD). In the case of the human I325N data, the structure was originally solved in space group P3₁2 with four molecules in the asymmetric unit. However, unaccounted-for electron density suggested a solution in the lower-symmetry P3₁ space group, with six molecules in the asymmetric unit, with sensible packing and no unaccounted-for density. The human wild-type A20 structure, solved as a control for iodoacetamide alkylation, also has six molecules (three dimers) in a different asymmetric unit and space group. The mouse OTU structure was solved in the P3₂ space group, with a dimer in the asymmetric unit. Restrained *B*-factor refinement, using local noncrystallographic symmetry restraints, was performed with REFMAC5 (ref. ⁶⁶).

For the mouse A20 OTU structure, torsion liberation screw parameterization and restrained refinement were carried out using phenix.refine⁶⁷. Between rounds of refinement, electron density maps and composite OMIT maps⁶⁸ and their fit to the model were examined. Amino acid side chains were added if suggested by difference map electron density. Difference maps identified the active site cysteine (C103) as the only cysteine residue alkylated by the iodoacetamide treatment in both human structures 5V3B and 5V3P (PDB residue descriptor YCM; for full list see <http://www.rcsb.org/pdb/results/results.do?tabtoshow=Current&grid=91A073F0>). The six molecules refined in each structure are highly similar in fold, both to themselves and as compared to each other. All molecules form dimers with neighboring molecules, as observed in other crystal structures. Structure validation was performed using the MOLPROBITY web server⁶⁹. The final human I325N, human wild-type and mouse wild-type structures contain Ramachandran-favored/outlier components of 88.64/0.00%, 88.13/2.87% and 82.13/7.87%, respectively.

Measurement of OTU domain thermal stability. Purified A20 OTU domains (0.4 mg ml⁻¹) were exchanged into 100 mM NaCl, 5 mM DL-Dithiothreitol and 20 mM Na₂HPO₄ (pH 7.5). Circular dichroism data were collected with a Chirascan circular dichroism spectrometer (Applied Photophysics) in a 1-mm cuvette. The protein was heated from 20–90 °C at a rate of 1 °C min⁻¹ while ellipticity was monitored at 220 nm. The thermally induced unfolding of A20 OTU domains was not reversible. The unfolding of the A20 OTU domains was described by a two-state model⁷⁰ (equation (1))

$$y_{\text{obs}} = \frac{y_n + m_n T + (y_u + m_u T) \exp\left(\frac{\Delta H_{\text{HT}}}{R} \left(\frac{1}{T} - \frac{1}{T_{\text{ts}}}\right)\right)}{1 + \exp\left(\frac{\Delta H_{\text{HT}}}{R} \left(\frac{1}{T} - \frac{1}{T_{\text{ts}}}\right)\right)} \quad (1)$$

where y_{obs} is the observed ellipticity and y_n and y_u are the ellipticity values observed for the native and unfolded states, respectively. The m_n and m_u values are the linear temperature dependencies of y_n and y_u . ΔH_{HT} is the apparent van't Hoff enthalpy, R is the universal gas constant and T_{ts} is the temperature at which the population of unfolded protein is 50%. Curves were fitted by nonlinear regression using GraphPad Prism v.6 (GraphPad Software).

Statistical methods. Results are expressed as mean \pm s.d. or mean \pm s.e.m. Statistical analysis was performed using Student's *t*-test, ANOVA or log-rank test, where indicated.

Reporting Summary. Further information on research design is available in the Nature Research Reporting Summary linked to this article.

Data availability

The data that support the findings of this study are available from the corresponding author upon reasonable request. PDB accession codes are 5V3P, 5V3B and 5DQ6.

References

- Siggs, O. M. et al. Preponderance of *CTLA4* variation associated with autosomal dominant immune dysregulation in the MYPPPY motif. *Front. Immunol.* **10**, 1544 (2019).
- Jacobs, G. S. et al. Multiple deeply divergent Denisovan ancestries in Papuans. *Am. J. Phys. Anthropol.* **168**, 112–112 (2019).
- Malaspinas, A. S. et al. A genomic history of Aboriginal Australia. *Nature* **538**, 207–214 (2016).
- Delaneau, O., Howie, B., Cox, A. J., Zagury, J. F. & Marchini, J. Haplotype estimation using sequencing reads. *Am. J. Hum. Genet.* **93**, 687–696 (2013).
- International HapMap Consortium. A second generation human haplotype map of over 3.1 million SNPs. *Nature* **449**, 851–861 (2007).
- Barrett, J. C., Fry, B., Maller, J. & Daly, M. J. Haploview: analysis and visualization of LD and haplotype maps. *Bioinformatics* **21**, 263–265 (2005).
- Ho, W. Y., Cooke, M. P., Goodnow, C. C. & Davis, M. M. Resting and anergic B cells are defective in CD28-dependent costimulation of naive CD4⁺ T cells. *J. Exp. Med.* **179**, 1539–1549 (1994).
- Akkraraju, S. et al. A range of CD4 T cell tolerance: partial inactivation to organ-specific antigen allows nondestructive thyroiditis or insulinitis. *Immunity* **7**, 255–271 (1997).
- Tahiliani, V., Chaudhri, G., Eldi, P. & Karupiah, G. The orchestrated functions of innate leukocytes and T cell subsets contribute to humoral immunity, virus control, and recovery from secondary poxvirus challenge. *J. Virol.* **87**, 3852–3861 (2013).
- Wang, G. G. et al. Quantitative production of macrophages or neutrophils *ex vivo* using conditional Hoxb8. *Nat. Methods* **3**, 287–293 (2006).
- Grey, S. T., Lock, J., Bach, F. H. & Ferran, C. Adenovirus-mediated gene transfer of A20 in murine islets inhibits Fas-induced apoptosis. *Transplant. Proc.* **33**, 577–578 (2001).
- Grey, S. T. et al. Genetic engineering of a suboptimal islet graft with A20 preserves beta cell mass and function. *J. Immunol.* **170**, 6250–6256 (2003).
- Untergasser, A. et al. Primer3: new capabilities and interfaces. *Nucleic Acids Res.* **40**, e115 (2012).
- Daley, S. R., Hu, D. Y. & Goodnow, C. C. Helios marks strongly autoreactive CD4⁺ T cells in two major waves of thymic deletion distinguished by induction of PD-1 or NF- κ B. *J. Exp. Med.* **210**, 269–285 (2013).
- Jeelall, Y. S. et al. Human lymphoma mutations reveal CARD11 as the switch between self-antigen-induced B cell death or proliferation and autoantibody production. *J. Exp. Med.* **209**, 1907–1917 (2012).
- Bendall, S. C. et al. Single-cell mass cytometry of differential immune and drug responses across a human hematopoietic continuum. *Science* **332**, 687–696 (2011).
- Qiu, P. et al. Extracting a cellular hierarchy from high-dimensional cytometry data with SPADE. *Nat. Biotechnol.* **29**, 886–891 (2011).
- Wertz, I. E. et al. Sensitivity to antitubulin chemotherapeutics is regulated by MCL1 and FBW7. *Nature* **471**, 110–114 (2011).
- Tan, B. M. et al. Baculoviral inhibitors of apoptosis repeat containing (BIRC) proteins fine-tune TNF-induced nuclear factor κ B and c-Jun N-terminal kinase signalling in mouse pancreatic beta cells. *Diabetologia* **56**, 520–532 (2013).
- Langley, D. B. & Christ, D. Crystal structure of duck egg lysozyme isoform II (DEL-II). *BMC Struct. Biol.* **18**, 10 (2018).
- McCoy, A. J. et al. Phaser crystallographic software. *J. Appl. Crystallogr.* **40**, 658–674 (2007).
- Murshudov, G. N. et al. REFMAC5 for the refinement of macromolecular crystal structures. *Acta Crystallogr. D Biol. Crystallogr.* **67**, 355–367 (2011).
- Adams, P. D. et al. PHENIX: a comprehensive Python-based system for macromolecular structure solution. *Acta Crystallogr. D Biol. Crystallogr.* **66**, 213–221 (2010).
- Terwilliger, T. C. et al. Iterative-build OMIT maps: map improvement by iterative model building and refinement without model bias. *Acta Crystallogr. D Biol. Crystallogr.* **64**, 515–524 (2008).
- Chen, V. B. et al. MolProbity: all-atom structure validation for macromolecular crystallography. *Acta Crystallogr. D Biol. Crystallogr.* **66**, 12–21 (2010).
- Zoldak, G., Zubrik, A., Musatov, A., Stupak, M. & Sedlak, E. Irreversible thermal denaturation of glucose oxidase from *Aspergillus niger* is the transition to the denatured state with residual structure. *J. Biol. Chem.* **279**, 47601–47609 (2004).

Reporting Summary

Nature Research wishes to improve the reproducibility of the work that we publish. This form provides structure for consistency and transparency in reporting. For further information on Nature Research policies, see [Authors & Referees](#) and the [Editorial Policy Checklist](#).

Statistics

For all statistical analyses, confirm that the following items are present in the figure legend, table legend, main text, or Methods section.

- | | |
|-----|-----------|
| n/a | Confirmed |
|-----|-----------|
- The exact sample size (n) for each experimental group/condition, given as a discrete number and unit of measurement
 - A statement on whether measurements were taken from distinct samples or whether the same sample was measured repeatedly
 - The statistical test(s) used AND whether they are one- or two-sided
Only common tests should be described solely by name; describe more complex techniques in the Methods section.
 - A description of all covariates tested
 - A description of any assumptions or corrections, such as tests of normality and adjustment for multiple comparisons
 - A full description of the statistical parameters including central tendency (e.g. means) or other basic estimates (e.g. regression coefficient) AND variation (e.g. standard deviation) or associated estimates of uncertainty (e.g. confidence intervals)
 - For null hypothesis testing, the test statistic (e.g. F , t , r) with confidence intervals, effect sizes, degrees of freedom and P value noted
Give P values as exact values whenever suitable.
 - For Bayesian analysis, information on the choice of priors and Markov chain Monte Carlo settings
 - For hierarchical and complex designs, identification of the appropriate level for tests and full reporting of outcomes
 - Estimates of effect sizes (e.g. Cohen's d , Pearson's r), indicating how they were calculated

Our web collection on [statistics for biologists](#) contains articles on many of the points above.

Software and code

Policy information about [availability of computer code](#)

Data collection

Data collection and specific references are detailed in Methods section.
 Flow Cytometry data was collected using BD FACS Diva Software Version 8.01 from BD BioScience.
 Histology images were collected on the Leica DM 4000 or Leica DM 6000 Power Mosaic microscopes.
 Luciferase assay data collected using a FLUOstar Omega plate reader.
 Mass cytometry data was collected using a CyTOF2 from Fluidigm.
 Mass spectrometry: Dionex UltiMate 3000 RSLCnano Proflow system was used from Thermo Fisher Scientific.
 Crystallographic data was collected at the Australian Synchrotron.
 Thermal stability: Chirascan circular dichroism spectrometer.
 qPCR analysis: LightCycler®480 Real Time PCR System (Roche)

Data analysis

Genome sequencing and population genetic analyses, were performed using tools described in the methods section.
 Mass cytometry: Spanning-tree Progression Analysis of Density-normalized Events (SPADE) analysis was used to resolve leukocyte lineages and subsets.
 Mass spectrometry: Tandem mass spectrometric data were searched against candidate sequences using Byonic and Byologic software packages (Protein Metrics Inc) and Areas under the curve were manually extracted from Xcalibur (Thermo Fisher Scientific).
 Crystallographic data: Data were indexed and integrated with MOSFLM. The spacegroups were scrutinized with POINTLESS, and the data scaled with AIMLESS, or SCALA accessed via the CCP4i software interface.
 Histology Images: Image J
 Graphpad Prism 7 was used for all graphical and statistical analysis.
 Treestar FlowJo 10.1 was used for analysis of flow cytometry and CyTOF files (FCS format).
 Microsoft Excel version 14.7.2.
 ImageJ v1.51 was used for densitometry and beta cell mass analysis.

For manuscripts utilizing custom algorithms or software that are central to the research but not yet described in published literature, software must be made available to editors/reviewers. We strongly encourage code deposition in a community repository (e.g. GitHub). See the Nature Research [guidelines for submitting code & software](#) for further information.

Data

Policy information about [availability of data](#)

All manuscripts must include a [data availability statement](#). This statement should provide the following information, where applicable:

- Accession codes, unique identifiers, or web links for publicly available datasets
- A list of figures that have associated raw data
- A description of any restrictions on data availability

The data supporting the findings of the study are available from the corresponding authors upon request.
PDB accession codes: PDB ID 5V3P and 5V3B.

Field-specific reporting

Please select the one below that is the best fit for your research. If you are not sure, read the appropriate sections before making your selection.

- Life sciences Behavioural & social sciences Ecological, evolutionary & environmental sciences

For a reference copy of the document with all sections, see [nature.com/documents/nr-reporting-summary-flat.pdf](https://www.nature.com/documents/nr-reporting-summary-flat.pdf)

Life sciences study design

All studies must disclose on these points even when the disclosure is negative.

Sample size	Sample sizes were determined based on previous studies and similar research reported in the literature to ensure adequate reproducibility of results. The sample size and associated statistics are indicated in the figures and respective legends..
Data exclusions	No data was excluded during analysis.
Replication	All biological experiments were repeated independently at least three times to ensure reproducibility of our findings. All attempt to replicate the reported experiment were successful.
Randomization	Experimental groups were not randomised. Age- and sex-matched animals were used for experiments, and littermates were used as controls where appropriate.
Blinding	The investigators were not blinded to group allocation during experiments and because we chose objective readouts and endpoints as measurements of experiments. Therefore the data were not prone to subjective evaluation. Conclusions were made based on 3 or more independent experiments, quantitative parameters and significance of the data.

Reporting for specific materials, systems and methods

We require information from authors about some types of materials, experimental systems and methods used in many studies. Here, indicate whether each material, system or method listed is relevant to your study. If you are not sure if a list item applies to your research, read the appropriate section before selecting a response.

Materials & experimental systems

n/a	Involved in the study
<input type="checkbox"/>	<input checked="" type="checkbox"/> Antibodies
<input type="checkbox"/>	<input checked="" type="checkbox"/> Eukaryotic cell lines
<input checked="" type="checkbox"/>	<input type="checkbox"/> Palaeontology
<input type="checkbox"/>	<input checked="" type="checkbox"/> Animals and other organisms
<input type="checkbox"/>	<input checked="" type="checkbox"/> Human research participants
<input checked="" type="checkbox"/>	<input type="checkbox"/> Clinical data

Methods

n/a	Involved in the study
<input checked="" type="checkbox"/>	<input type="checkbox"/> ChIP-seq
<input type="checkbox"/>	<input checked="" type="checkbox"/> Flow cytometry
<input checked="" type="checkbox"/>	<input type="checkbox"/> MRI-based neuroimaging

Antibodies

Antibodies used

Antibodies for Western blotting and immunoprecipitation:
Antibodies from Cell Signaling Technology:
anti-A20 (Prod#: 5630; clone: D13H3), anti-IkB α (prod#: 9242), anti-phospho-IkB α (prod#: 9246; clone: 5A5), anti-IkK β (2684), anti-JNK (9252), anti-phospho-JNK (Prod#: 9255; clone: G9), anti-IkK α (Prod#: 2682), anti-phospho-IkK α/β (Prod#: 2697; clone: 16A6), anti-phospho-TAK1 (Prod#: 4536; clone: 90C7); anti-TAK1 (Prod# 5206; clone:D94D7), anti-TNFR1 (Prod#: 3736; clone: C25C1) , anti-NIK (Prod#: 4994), anti-NF- κ B2 p100/p52 (Prod#: 4882), anti-RelB (Prod#: 4922; clone: C1E4), anti-insulin (Prod# 4590).
Antibodies from Sigma-Aldrich:

anti-beta-actin (Prod# A1978; clone: AC15)
 Antibodies from Pierce Antibodies:
 HRP-labeled goat-anti-mouse IgG Fc (Prod#: 31433; lot # HJ10361912)
 Antibodies from GE Life Sciences:
 HRP-labeled donkey-anti-rabbit IgG (Prod#: NA934V; lot # 9790788)
 Antibodies from abcam:
 anti-TNFR1 (Prod#: ab7365), anti-A20 (prod#: 59A426)
 Antibodies from Santa Cruz:
 anti-RIP1 (Prod#: sc-7881; clone: H-207), anti-A20 (Prod#: sc-166692; clone: A-12), anti-ubiquitin (prod#: sc-8017; clone: P4D1)
 Antibodies from BD bioscience:
 anti-RIP1 (Prod#: 610458; clone: 38/RIP)
 Dako: HRP-labelled polymer-conjugated goat anti-rabbit IgG (#K4002).
 Antibodies used for flow cytometry (mouse):
 Purchased from BD, eBioscience, BioLegend BD or Invitrogen (outlined further in methods):
 CD4 (clone: RM4-5), CD8 (clone: 53-6.7), CD21 (clone: 7G6), CD23 (clone: B3B4), CD25 (clone: PC61.5), CD44 (clone: IM7), CD69 (clone: H1.2F3), CD93 (clone: AA.4.1), CD45.2 (clone: 104), B220 (clone: RA3-6B2), IgM (clone: II/41), IgD (clone: 11-26), FOXP3 (FJK-165).
 Antibodies used for flow cytometry (human):
 Purchased from BD, eBioscience, BioLegend BD or Invitrogen:
 anti-CD3 (UCHT1), anti-CD4 (SK3), anti-CD8 (RPA-T8); anti-CD127 (A019D5), anti-CCR7 (CD197); anti-CD25 (2A3), and anti-CD45RA PerCP-Cy5.5 (HI100)

anti-S381-A20, used for western blotting was a kind gift by Professor Derek W. Abbott. DOI: 10.1128/MCB.01101-07

Validation

All antibodies (besides anti-S381-A20) are from commercial sources and have been validated by the vendors on their official website. Further details can be found at:
 Cell Signaling Technology: <https://www.cellsignal.com/contents/our-approach/cst-antibody-validation-principles/ourapproach-validation-principles>
 Biolegend: <https://www.biolegend.com/reproducibility>
 BD: <http://bdbiosciences.com/us/support/s/technicalsupport>
 Santa Cruz Biotechnology: <https://www.scbt.com/scbt/resources/technical-service>
 All antibodies against surface-expressed markers used in this study have been previously validated by the manufacturer, as stated on their associated product webpages, and by our own lab in previous experiments and in positive/negative controls for expected staining pattern.

Eukaryotic cell lines

Policy information about [cell lines](#)

Cell line source(s)	American Tissue Culture Collection. beta-tc3 and HEK293T cell lines were used in this study.
Authentication	BTC3 and HEK293 are well established cell lines. Authentication were performed by morphology. Cell lines were monitored regularly for growth characteristics and cell morphology.
Mycoplasma contamination	Cell lines tested negative for mycoplasma contamination; all cells grew well and health/viability was checked prior to each experiment.
Commonly misidentified lines (See ICLAC register)	No commonly misidentified cell lines were used.

Animals and other organisms

Policy information about [studies involving animals](#); [ARRIVE guidelines](#) recommended for reporting animal research

Laboratory animals	Female and male mice were used as indicated. Age of mice used were between 6-12 weeks unless specified. Genetically modified C57/BL6 mice were used in this study with WT littermates used as controls. The Tnfaip3 Lasvegas strain (Tnfaip31325N) were generated by N-ethyl-N-nitrosourea (ENU) mutagenesis of C57BL/6 mice, and propagated by backcrossing to C57BL/6. Tnfaip3C243Y and I207L mice, were generated as described in methods. Founder mice carrying the C243Y substitution were then crossed to C57BL/6. Tnfaip3C103A (doi:10.1038/nature16165), 3A9 TCR transgenic (doi: 10.1084/jem.179.5.1539) and insHEL transgenic (doi: https://doi.org/10.1016/S1074-7613(00)80528-2) mice have been described.
Wild animals	Study did not involve wild animals.
Field-collected samples	Study did not involve samples collected from the field.
Ethics oversight	Animal studies were approved by the Garvan/St Vincent's or the Australian National University Animal Ethics Committees. All procedures performed complied with the Australian Code of Practice for Care and Use of Animals for Scientific Purposes.

Note that full information on the approval of the study protocol must also be provided in the manuscript.

Human research participants

Policy information about [studies involving human research participants](#)

Population characteristics	Patients and healthy family members were recruited via the Clinical Immunogenomics Research Consortium Australia (CIRCA) and The Children's Hospital at Westmead providing written informed consent under the protocols approved by relevant human research ethics boards. Blood samples from healthy volunteers were obtained from the Australian Red Cross Blood Service.
Recruitment	Patients and healthy family members were recruited via the Clinical Immunogenomics Research Consortium Australia (CIRCA) and The Children's Hospital at Westmead. Blood samples from healthy volunteers were obtained from the Australian Red Cross Blood Service.
Ethics oversight	All protocols were approved by the St. Vincent's Hospital Human ethics board (HREC). All patients provided written informed consent.

Note that full information on the approval of the study protocol must also be provided in the manuscript.

Flow Cytometry

Plots

Confirm that:

- The axis labels state the marker and fluorochrome used (e.g. CD4-FITC).
- The axis scales are clearly visible. Include numbers along axes only for bottom left plot of group (a 'group' is an analysis of identical markers).
- All plots are contour plots with outliers or pseudocolor plots.
- A numerical value for number of cells or percentage (with statistics) is provided.

Methodology

Sample preparation	Samples for flow cytometry were performed as described in the methods section.
Instrument	Data were collected on LSR II flow cytometers (BD).
Software	Data were analyzed using FlowJo software (Tree Star).
Cell population abundance	Cell sorting was not performed in this study
Gating strategy	Based on cell size (forward scatter, FSC) and cell granularity (sideward scatter, SSC), cell debris were excluded from cells. Subsequently, FCS and SSC doublets were excluded. Cell debris, doublets and dead cell exclusion were applied in all flow cytometry analysis. A gating strategy for human PBMCs is provided (Supplementary Figure 16). Mouse gating strategies are defined in relevant figure legends.

- Tick this box to confirm that a figure exemplifying the gating strategy is provided in the Supplementary Information.